Project No. 11-3247

In-Pile Instrumentation Multi-Parameter System Utilizing Photonic Fibers and Nanovision

Fuel Cycle Research and Development

Eric Burgett
Idaho State University

In collaboration with:
University of Maryland

Frank Goldner, Federal POC
Keith Jewell, Technical POC

NEUP Nuclear Energy University Programs
U.S. Department of Energy

Idaho State University

921 South 8th Ave. Stop 8060
Pocatello, ID, 83209-8060
Phone: 2028-282-2220
Email: burgeric@isu.edu

NanoVision

Final Report

October 2015

[Intentional Blank Page]

Approved By:

_____

Dr. Eric Burgett, Idaho State University

_____

Dr. Christopher Summers, Georgia Institute of Technology

_____

Dr. Mohamad Al-Sheikhly, University of Maryland

[Intentional Blank Page]

Table of Contents

INTRODUCTION 9

PROPOSED SCOPE DESCRIPTION 9

CURENT STATUS : 10

DELIVERABLE #1 DOCUMENT REPORTING THE COMMISSIONING AND INITIAL GROWTH QUALITY OF THE NEW ALD SYSTEM PROVIDED TO DOE. 10
DELIVERABLE #2 DOCUMENT REPORTING FIB COMMISSIONING 10
DELIVERABLE #3 DOCUMENT REPORTING FIRST NANOVISION SENSOR PERFORMANCE. 10
DELIVERABLE #4 DOCUMENT REPORTING STRESS/STRAIN/COMPRESSION SENSOR PERFORMANCE. 15
DELIVERABLE #5 DOCUMENT REPORTING THE CALIBRATION DATA FOR THE FIRST NANOVISION DEVICES. 39
DELIVERABLE #6 DOCUMENT REPORTING THE FIRST RADIATION TESTS DEVELOPED. 42
DELIVERABLE #7 DOCUMENT REPORTING THE FIRST FUEL BASED RADIATION TESTS DEVELOPED. 43
DELIVERABLE #8 DOCUMENT REPORTING THE PERFORMANCE OF CALIBRATED VERSIONS OF NANOVISION DEVELOPED. 43
DELIVERABLE #9 DOCUMENT REPORTING THE PERFORMANCE OF CALIBRATED VERSIONS OF NANOVISION ON FUEL DEVELOPED. 43
DELIVERABLE #10 FINAL REPORT. 44
DELIVERABLE #11 QUARTERLY REPORTS. 44
DELIVERABLE #12 YEARLY REPORTS. 44
DELIVERABLE #13 CONSULT WITH OUTSIDE INDUSTRY PARTNERS FOR COMMERCIALIZATION. 44

STUDENTS 44

BUDGET DATA 44

REFERENCES: 45

APPENDIX A – ADDITIONAL INTENSITY GRAPHS 46

Table of Figures

Figure 1 - An etched photonic crystal structure in the surface of a ceria surrogate. The triangular pitch was etched with a focused ion beam microscope. 10

Figure 2 - Comparison of intensity results 12

Figure 3 - Returned wavelength vs. temperature of a photonic crystal on silicon 12

Figure 4 - Wavelength vs. temperature from run 3 with 95% uncertainty bands 13

Figure 5 - Silicon coefficient of thermal expansion vs. temperature data and fit with 95% uncertainty bands 13

Figure 6 - Silicon Coefficient of Thermal Expansion vs. Wavelength 14

Figure 7 - Silicon Thermal Strain vs. Wavelength 14

Figure 8 – A honeycomb lattice showing deformation under various strains 16

Figure 9 - Band gap intensity graph for a honeycomb structure on silicon, n~4.162, r~0.176 16

Figure 10 - Complete band gap intensity graph for a honeycomb structure on silicon, n~4.162, R~0.176 17

Figure 11 - Band Gap Intensity graph for triangular lattice on silicon, N~4.162, R~0.42 17

Figure 12 - Complete band gap intensity graph for triangular lattice on silicon, n~4.162, r~0.42 18

Figure 13 - Band gap intensity graph for honeycomb lattice on UO2, n~ 2.92, r~0.27 18

Figure 14 - Complete band gap intensity graph for honeycomb lattice on uo2, n~2.92, r~0.27 19

Figure 15 - Expected total gap return at various strains on a honeycomb lattice, steel, r 0.27, n 2.92 19

Figure 16 - Expected tm4 return at various strains on a honeycomb lattice, steel, r 0.27, n 2.92 20

Figure 17 - Change in TE1 band gap wavelength as a result of isotropic strain (such as would be caused by thermal expansion), in a square lattice of square rods on steel 20

Figure 18 - Line defects in a square lattice of square rods 21

Figure 19 - Results from line defect simulations. If material is assumed to be perfectly non-absorbent, reflection will be the inverse of this graph 21

Figure 20 - Honeycomb lattice test 22

Figure 21 - Beam shift grid 22

Figure 22 - Square lattice of round rods 23

Figure 23 - Square lattice, 45 degree tilt, note rod-like structure 23

Figure 24 - Honeycomb lattice on steel with beam shift, note overlap 25

Figure 25 – Large pattern, note cyclic drift 25
Figure 26 - Square lattice of holes 25
Figure 27 - Square lattice of pillars, epsilon map from MPB 26
Figure 28 - Cross section of square pillars in steel, 45 degree tilt 26
Figure 29 - Square pillars on steel, 45 degree tilt 26
Figure 30 - Square pillars on steel, 90 degree rotation, 45 degree tilt 27
Figure 31 - Square pillars on steel 27
Figure 32 - Array of square lattice crystals 27
Figure 33 - Array of square lattice crystals 27
Figure 34 - Photonic crystal array in steel under direct top-lighting 28
Figure 35 - Photonic Effect Under Side Lighting Of A Crystal Array In Steel 28
Figure 36 - Photonic effect under side lighting of a crystal array in steel 29
Figure 37 - Photonic effect under side lighting of a crystal array in steel 29
Figure 38 - A 150um square 1-D photonic crystal 30
Figure 39 - A 2x2 array of 15x15 arrays of 5um photonic crystals 30
Figure 40 - large Bragg Grating on steel (~450x150um). left: top light, right: side light 31
Figure 41 - Graph showing bragg grating return vs indenter position 31
Figure 42 - 10x10 array of 5um Green optimized PCs on steel 32
Figure 43 - Spectrophotometer results for a green optimized PC on steel 32
Figure 44 – Spectrophotometer result for a green optimized PC on steel plus gaussian approximation 33
Figure 45 - Diagram showing the three ends of a reflection probe fiber. The sample end uses a single fiber fitting to both illuminate and measure the sample. 34
Figure 46 - Green return from a Zircaloy-4 PC using the single-bundle interrogation technique. The peak has an approximate FWHM of 11nm, and an approximate center wavelength of 529nm 34
Figure 47 - A group of four 5x5um photonic crystals on UO2 35
Figure 48 - The same group of four 5x5um photonic crystals as in Figure 46, illuminated under three different lighting angles, with histograms 36
Figure 49 - Zircaloy-4 photonic crystal, optical microscopy with histograms. 36
Figure 50 – Top light optical micrograph of an early milling depth reduction test 37

Figure 51 - Side light optical micrograph of an early milling depth reduction experiment. Note that the return on 300nm and 100nm crystals appears similar 37

Figure 52 - Rods in silicon through platinum mask 38

Figure 53 - Rods in silicon through platinum mask, 45 degree tilt 38

Figure 54 - Cross section of rods in silicon through platinum mask, 45 degree tilt 39

Figure 55 - Phidget board 39

Figure 56 - Dog bone micro-tensile sample 39

Figure 57 - Custom tensile tester 40

Figure 58 - Load cell calibration test 40

Figure 59 - Stress strain curve for steel micro-tensile sample 41

Figure 60 - High resolution FIB mosaic image of post-irradiation photonic crystal on steel. Gross mechanical damage is readily apparent 42

Figure 61 - Optical micrograph of post-irradiation PC. Top light at left, side light at right 43

Introduction

An advanced in-pile multi-parameter reactor monitoring system is being proposed in this funding opportunity. The proposed effort brings cutting edge, high fidelity optical measurement systems into the reactor environment in an unprecedented fashion, including in-core, in-cladding and in-fuel pellet itself. Unlike instrumented leads, the proposed system provides a unique solution to a multi-parameter monitoring need in core while being minimally intrusive in the reactor core. Detector designs proposed herein can monitor fuel compression and expansion in both the radial and axial dimensions as well as monitor linear power profiles and fission rates during the operation of the reactor. In addition to pressure, stress, strain, compression, neutron flux, neutron spectra, and temperature can be observed inside the fuel bundle and fuel rod using the proposed system. The proposed research aims at developing radiation hard, harsh environment multi-parameter systems for insertion into the reactor environment. The proposed research holds the potential to drastically increase the fidelity and precision of in-core instrumentation with little or no impact in the neutron economy in the reactor environment while providing a measurement system capable of operation for entire operating cycles.

Proposed Scope Description

Advancing the fuel cycle requires advancements in our basic understanding of fuel behavior under irradiation. Investments are being made in advanced modeling and simulation to predict in-pile behavior and as the tool for innovative fuel design. These new models will require novel data to not only benchmark key calculations but to actually guide their development. The required data will need to be of unprecedented precision and granularity. To further complicate the delivery of these data, some of the most interesting measurements will need to be made in-pile during the first few hours of irradiation. These sensitive new measurements may require novel systems to collect, package and send data from in-pile sensors to remote data acquisition systems, which must be maintained well outside the neutron radiation field. Delivering this high precision, in-pile data is a daunting task and we propose to take the first necessary steps in developing a viable research and development effort to meet these challenges.

Early in the fuel's life in a reactor, significant changes in the fuel meat grain structure occur that impact performance through the life of the fuel. A significant effort to model these phenomena is underway in the Fuel Cycle R&D program. These atomistic to macroscopic models utilize many different data models for fuel pellet behavior. However, beginning of life data is currently limited to millimeter scale and larger for defects and grain boundary changes. It may be possible to measure fuel sample deformations with a novel monitoring system that utilizes an embedded photonic crystal structure. This novel technique that we refer to as "NanoVision", utilizes the photonic crystal structure in a completely new fashion in order to yield information on real time fuel changes on the scale of nanometers as opposed to millimeters. It becomes possible to measure nearly atomistic changes in real-time during irradiation. NanoVision provides a unique monitoring capability which can be applied to fuel materials, cladding materials, any material in which more precise information over grain swelling, grain compression, temperature, crack formation and propagation is desired in two or three dimensions. This system provides unprecedented accuracy (nm scale deformations) and can do it in a repeatable fashion using nanotechnology.

The proposed research is designed to monitor several key parameters in fuel performance. The parameters of concern which NanoVision is optimally designed for is pellet swelling, pellet compression, grain reformation, crystal reorientation/restructuring, temperature and crystal separation. This is an initial list of parameters that can be monitored in three dimensions with NanoVision. These parameters can be created from three distinct versions of NanoVision which all center on the photonic crystal structure.

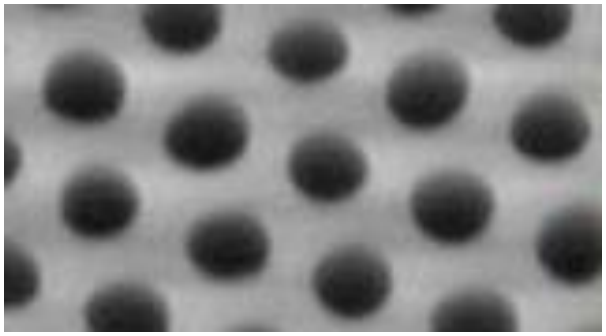

FIGURE 1 - AN ETCHED PHOTONIC CRYSTAL STRUCTURE IN THE SURFACE OF A CERIA SURROGATE. THE TRIANGULAR PITCH WAS ETCHED WITH A FOCUSED ION BEAM MICROSCOPE.

Current Status:

Deliverable #1 Document reporting the commissioning and initial growth quality of the new ALD system provided to DOE.

Milestone #1: Commission ALD System

Deliverable #1: (Participants) ISU

Deliverable #1: (Status) The ALD tool was vetted through the standing QA/QC purchasing requirements of the RISE Complex. ALD has been purchased. It has been shipped to ISU. The unit was damaged in shipment. A forklift was run through the side of the unit. The university has filed a claim with the shipping company. Repairs have begun and have continued this quarter. Repairs are expected to be completed this upcoming quarter, during July.

Deliverable #2 Document reporting FIB Commissioning.

Milestone #2: Commissioning of the Focused Ion Beam system.

Deliverable #2: (Participants) ISU

Deliverable #2: (Status) The FIB is on-site and functional. Work has progressed in the milling script for autocorrecting drift and astigmatism during operation. This has resulted in large photonic structures. A document reporting the commissioning will follow in the upcoming quarter.

Deliverable #3 Document reporting first NanoVision sensor performance.

Milestone #3: Grow first NanoVision Photonic Crystals.

Deliverable #3: (Participants) ISU

Deliverable #3: (Status) Photonic crystal band gap (PCBG) studies of unstrained systems have begun. Experimentation on production of photonic crystals in various materials is underway. Test procedures have been created at the University of Maryland and are in use at Idaho State University.

A LEOI-100 Experimental CCD Spectrometer will be used for analyzing wavelengths of light returned from photonic crystals. By comparing the wavelength of light returned from the sample under strain to the original wavelength returned from the un-deformed photonic crystal a relation between strain and wavelength return can be created. To measure two dimensional deformation polarized light will be directed onto the sample and the change in the returned light in both dimensions can be measured.

The spectrometer must be calibrated before use. Calibration is achieved by using light sources of well-known wavelengths as the calibration points for a linear calibration. A minimum of two wavelengths are required for a linear calibration, with increased accuracy with greater numbers of wavelengths and the farther those wavelengths are apart. High levels of accuracy have been achieved using vapor lamps, including mercury, sodium, hydrogen, and neon. Reasonable accuracy using small numbers of laser lights has also been achieved. The spectrometer can only be calibrated over a range of ~200 nanometers, therefore requiring all calibration sources to be within the ~200 nm range of interest.

The spectrometer was initially calibrated using a monochromator, with significant improvement using a combination of a monochromator and both neon and sodium vapor lamps. Farther improvements in accuracy have been achieved using helium and mercury atomic vapor lamps without a monochromator. These current calibration techniques have been producing significantly higher accuracy results than previous methods.

TABLE 1 - UPDATED CALIBRATION RESULTS

Calibration	Average Error in Measurements
Initial	1.44 nm
Last Quarter	0.53 nm
Current	0.022 nm

Changes in techniques and optical connections have significantly improved the brightness of the light returned from the photonic crystal into fiber optic cables, which will be used in the envisioned NanoVision deployment scenario.

These improvements were made by using a thick cored light delivery cable, a collimator on both ends of the delivery cable, and two lenses to better focus light into the delivery cable. Farther improvements will allow the use of smaller cables, which will more easily fit into small spaces, such as a reactor core. Farther improvements will be pursued by using a brighter light source and focal lenses designed for fiber optic cables.

Method	Returned Intensity
Initial	80
Current	5000

TABLE 2 - UPDATED RETURNED INTENSITY RESULTS

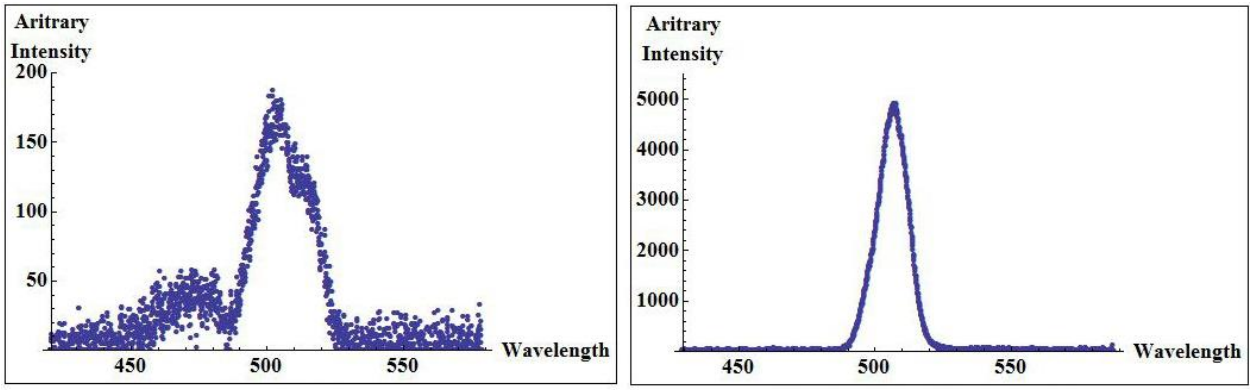

Light intensity returned from a photonic crystal, old method

Light intensity returned from a photonic crystal, new method

FIGURE 2 - COMPARISON OF INTENSITY RESULTS

A thermal couple is being used to measure the temperature of the photonic crystal for wavelength vs. temperature experiments. Testing the wavelength shift of returned light compared to the temperature of the photonic crystal has shown a clear relationship between wavelength and temperature. This can be seen in Figure 3, including 95% uncertainty bands.

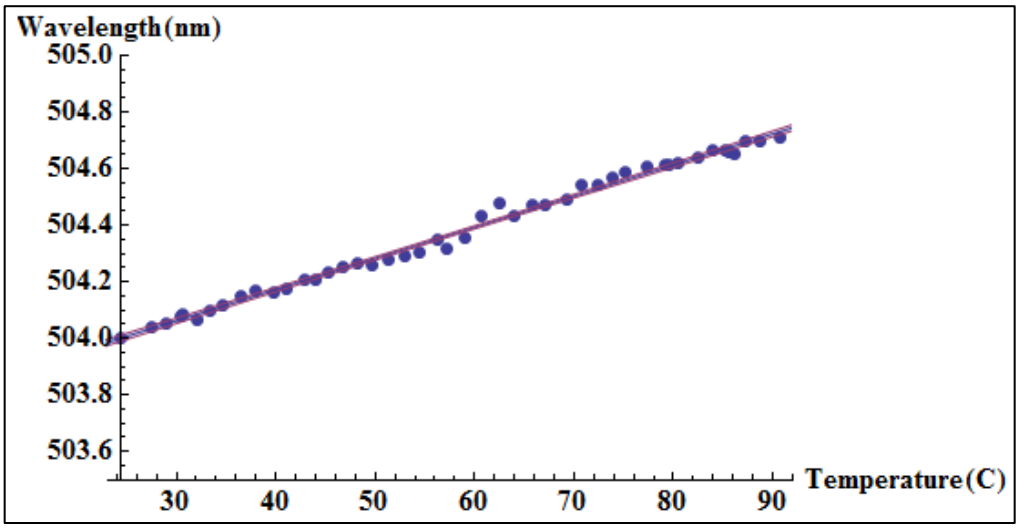

FIGURE 3 - RETURNED WAVELENGTH VS. TEMPERATURE OF A PHOTONIC CRYSTAL ON SILICON

Comparing multiple tests at the same geometry has determined slopes for the wavelength vs. temperature relation. Although the numbers can only apply to one specific geometry (sensor and light position), they are repeatable for that geometry. Further improvements will be made to the system by increasing the steadiness of the optical equipment, photonic crystal, and thermal couple. This will make the system more resistant to physical disturbances and will allow greater optimization of geometries. A brighter and whiter light source

will be used to increase the returned brightness which will allow smaller fiber optic cables to be used and to ensure there are no preferred wavelengths from the light source. Attaching the system to a microscope and high precision stage will allow measurement of smaller features and offer improved repeatability.

For light incident on a photonic crystal on silicon, the wavelength of the returned light vs. the temperature of the photonic crystal can been seen in Figure 4. A high correlation between wavelength and low uncertainty can be seen comparing the data points to the fitted line and 95% uncertainty bands in Figure 4.

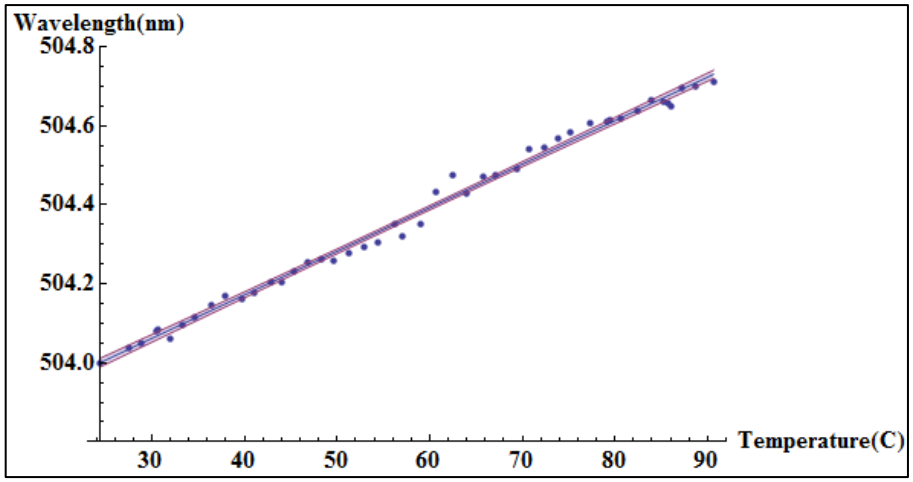

FIGURE 4 - WAVELENGTH VS. TEMPERATURE FROM RUN 3 WITH 95% UNCERTAINTY BANDS

Collecting thermal expansion data for silicon, the photonic crystal material, and then fitting a line to the data based on temperature, a reasonable correlation between the coefficient of thermal expansion and temperature can be seen in Figure 5.

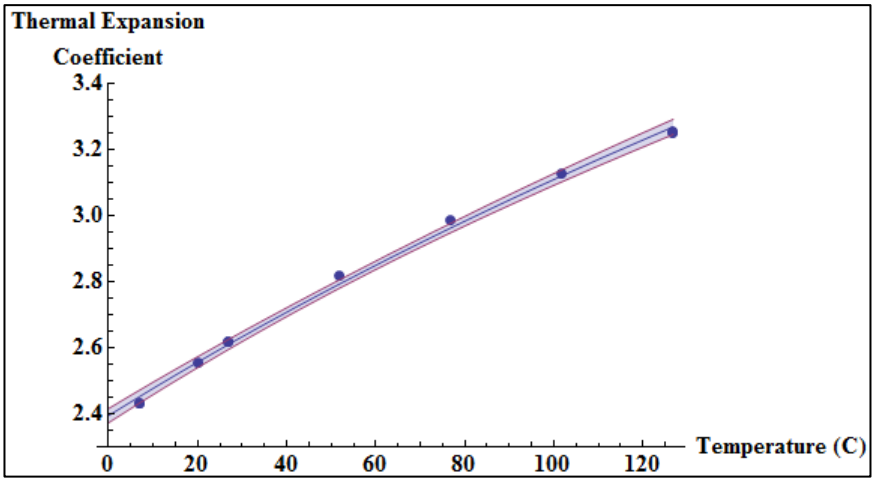

FIGURE 5 - SILICON COEFFICIENT OF THERMAL EXPANSION VS. TEMPERATURE DATA AND FIT WITH 95% UNCERTAINTY BANDS

Since the coefficient of thermal expansion and wavelength are both functions of temperature, the coefficient of thermal expansion can be expressed as a function of wavelength, as can be seen in Figure 6.

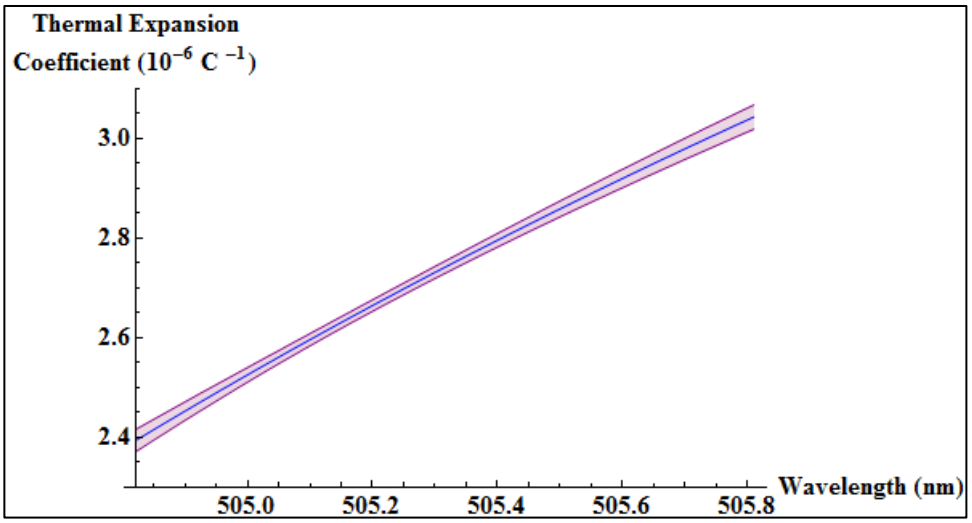

FIGURE 6 - SILICON COEFFICIENT OF THERMAL EXPANSION VS. WAVELENGTH

Strain can also be related to thermal expansion, allowing strain to be calculated as a function of wavelength, as can be seen in Figure 7.

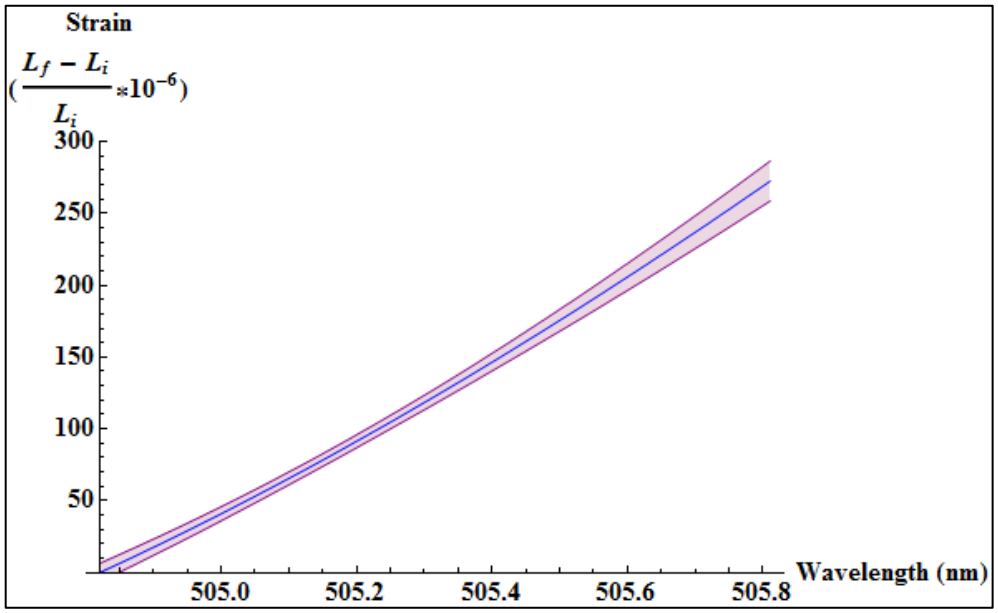

FIGURE 7 - SILICON THERMAL STRAIN VS. WAVELENGTH

These calculations show that it is theoretically possible that strain can be accurately determined from wavelength measurements. These measurements demonstrate a measureable relationship between temperature and wavelength, proving that photonic crystals can be used as a temperature sensor. A simple equation

relating temperature to wavelength for this test crystal is shown below. Note that this equation is specific to the calibration range in which the experiment was carried out.

$$T = \frac{\lambda - 504.819}{0.01106}$$

Deliverable #4 Document reporting stress/strain/compression sensor performance.

Milestone #4: Develop the first stress-strain-compression PCF.

Deliverable #4: (Participants) ISU

Deliverable #4: (Status)

Summary

Simulation of various lattice types in several materials has been completed. Further work on production of crystal arrays via FIB has taken place since the previous quarterly report. Drift during milling still occurs and appears to be a hardware issue. To correct for this, custom drift correction software has been designed and is continually being improved. Large arrays of smaller crystals have been successfully produced in order to help circumvent milling drift issues. Very large arrays (greater than 30 um on a side) will not be feasible to mass produce in the FIB, so alternate production methods are being investigated.

Simulation

Various lattices have been simulated on iron, UO2 and silicon. Additionally, the effect of strain on an iron honeycomb lattice has been roughly simulated in MPB.

For the simulation of photonic crystals on UO2 and Si, MPB (MIT photonic bands) was used. Values for the index of refraction of UO2 do not appear to be readily available, and literature searches have yielded a significant variance in reported values. For these simulations, a range of n values were used. Data for n 2.75 is shown in this report.

To attempt to simulate the effect of strain on a photonic crystal, it is necessary to be able to deform the crystal by varying amounts. Since MBP does not appear to possess built in code for deforming a lattice, it was decided to instead to use a lattice of elliptical holes, which allows the minor and major axes to be separately adjusted. Thus with the axes equal, the lattice remains circular. A control file has been written which requires as basic inputs the Poisson ratio, strain percent and original dimensions of the ellipse. The strain direction is assumed to be along the major axis of the ellipse. Based on said inputs, the control file can then calculate the deformed ellipse dimensions. Shown below is a honeycomb lattice under various strains.

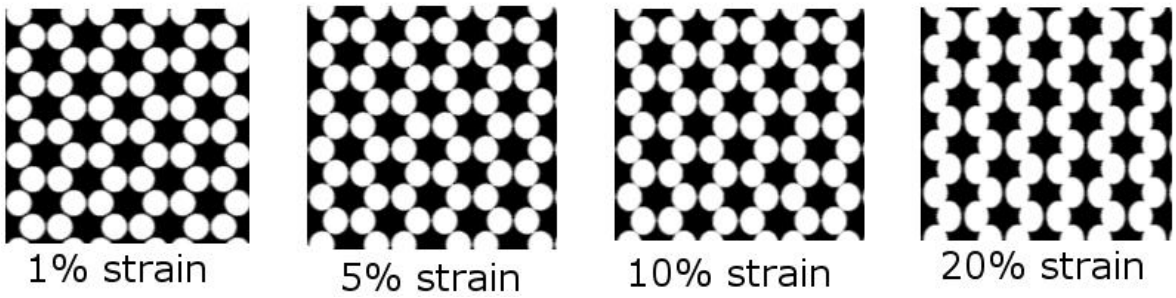

FIGURE 8 - A HONEYCOMB LATTICE SHOWING DEFORMATION UNDER VARIOUS STRAINS

Once again the scale invariant property of the Maxwell Equations is exploited to optimize these crystals to return at 540 nm. Indices of refraction at 540 nm were used to run the simulations. The honeycomb structure remains of particular interest because it possesses a total band gap on both UO2 and silicon. However, a complete band gap was also found with a triangular lattice on silicon.

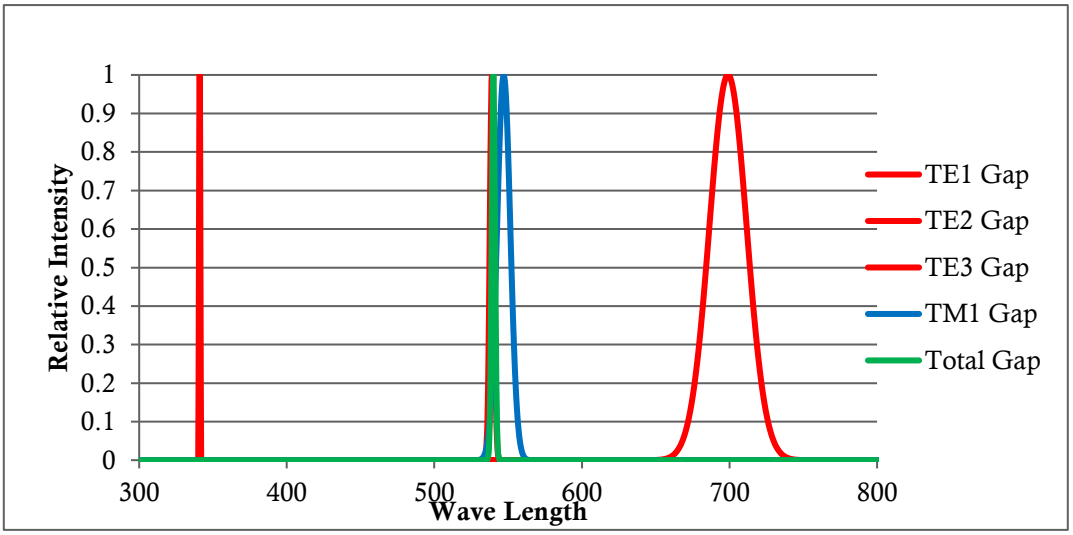

FIGURE 9 - BAND GAP INTENSITY GRAPH FOR A HONEYCOMB STRUCTURE ON SILICON, N~4.162, R~0.176

For a honeycomb lattice in iron, it was found that there was a complete band gap with a width of approximately 9 nm (see January 2012 quarterly report for details.) When simulating a deformed lattice, it was found that for this structure, the total band gap disappears somewhere between 5% and 10% strain. The change in the peak wavelength is approximately 1nm at 1% and 8nm at 5% strain.

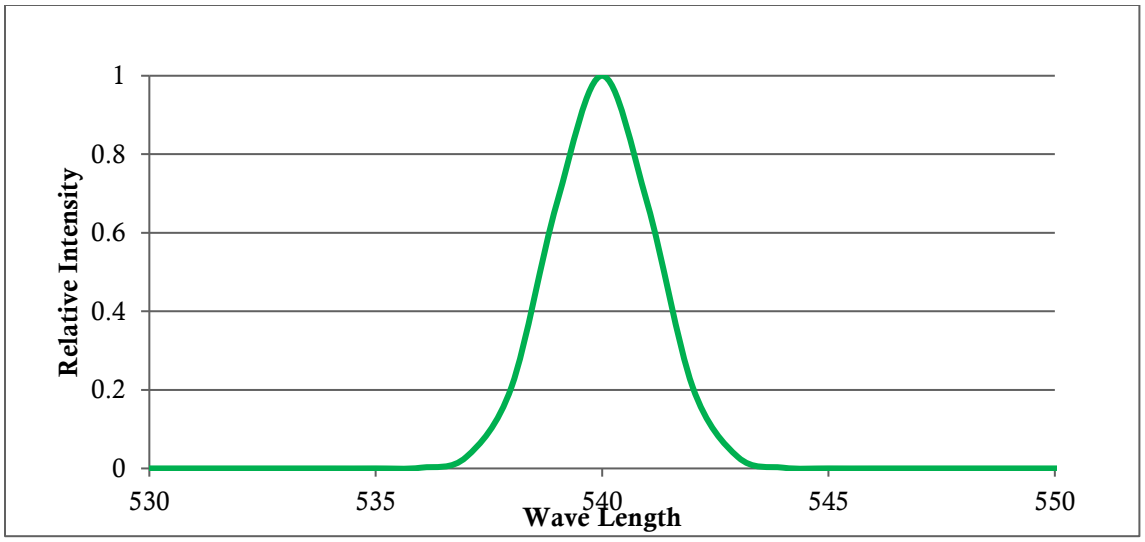

FIGURE 10 - COMPLETE BAND GAP INTENSITY GRAPH FOR A HONEYCOMB STRUCTURE ON SILICON, N~4.162, R~0.176

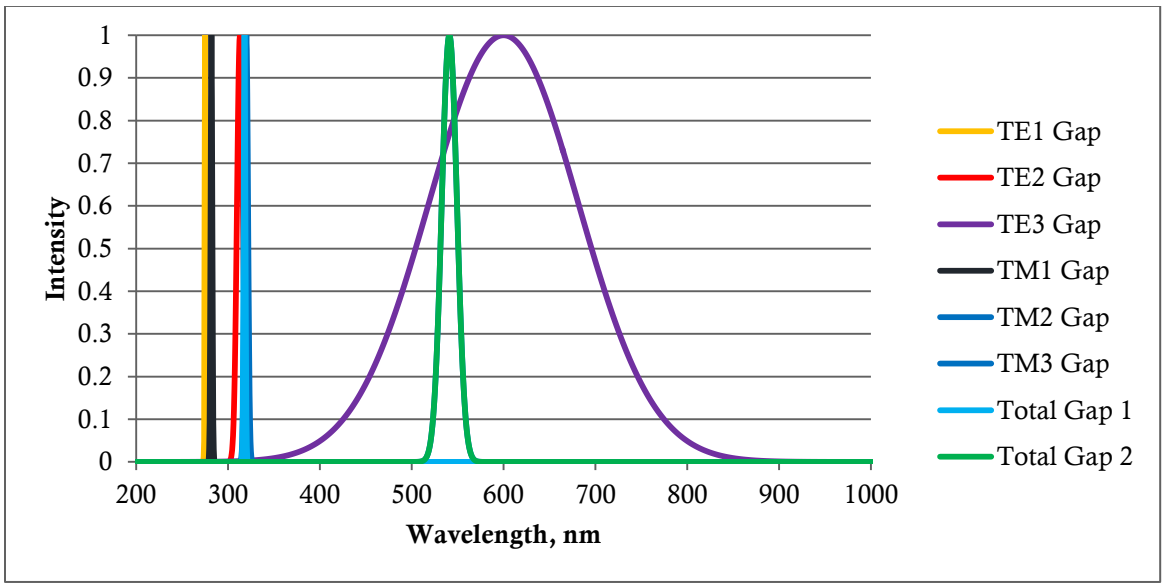

FIGURE 11 - BAND GAP INTENSITY GRAPH FOR TRIANGULAR LATTICE ON SILICON, N~4.162, R~0.42

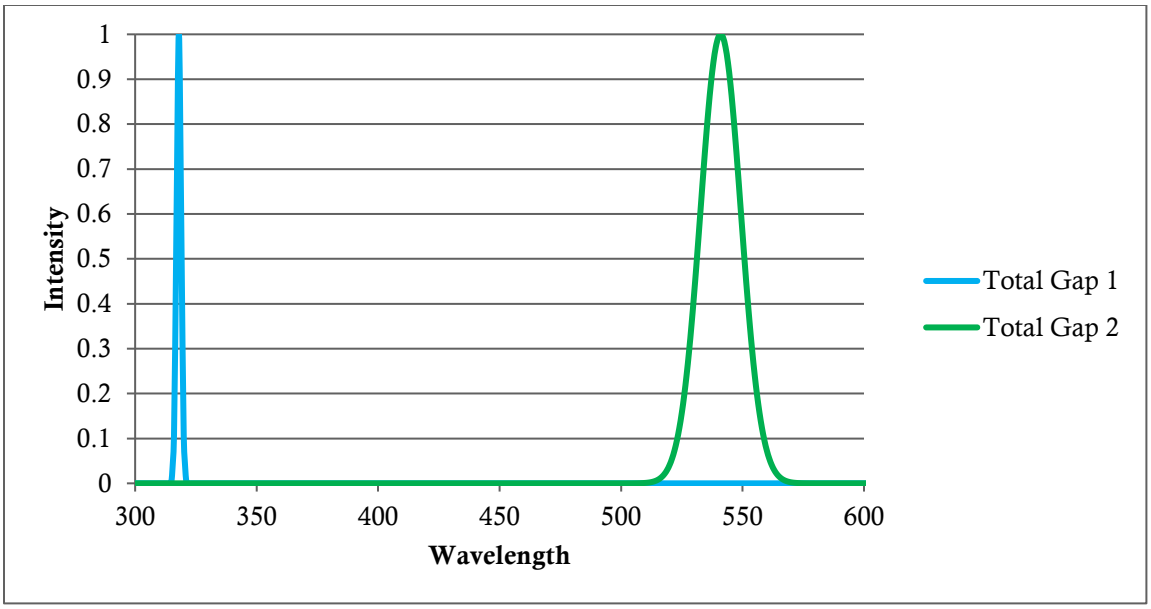

FIGURE 12 - COMPLETE BAND GAP INTENSITY GRAPH FOR TRIANGULAR LATTICE ON SILICON, N~4.162, R~0.42

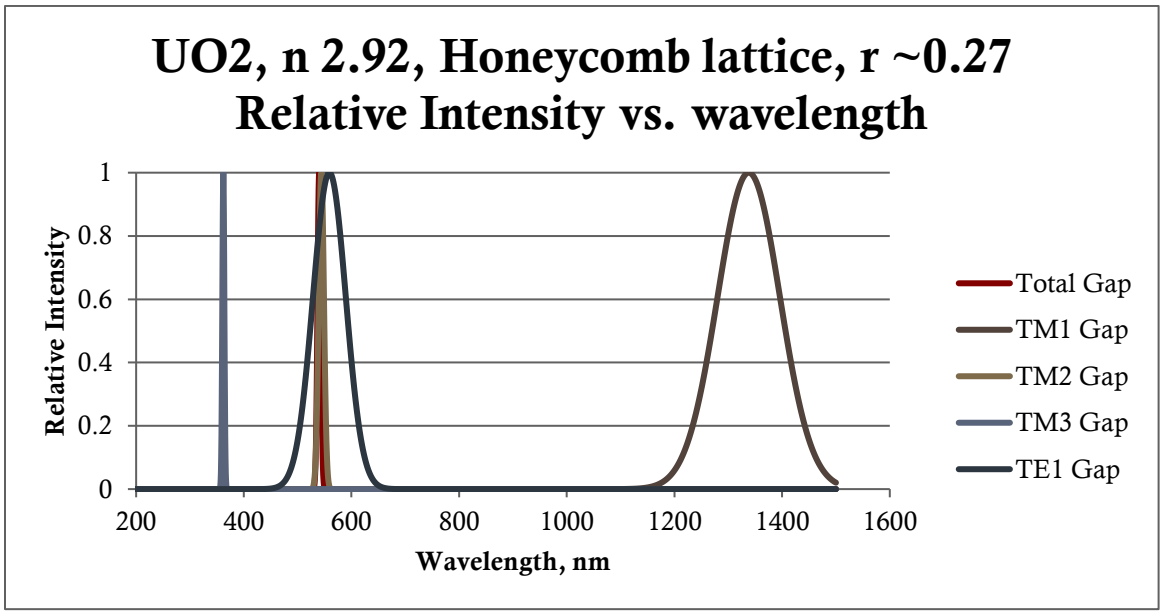

FIGURE 13 - BAND GAP INTENSITY GRAPH FOR HONEYCOMB LATTICE ON UO2, N~ 2.92, R~0.27

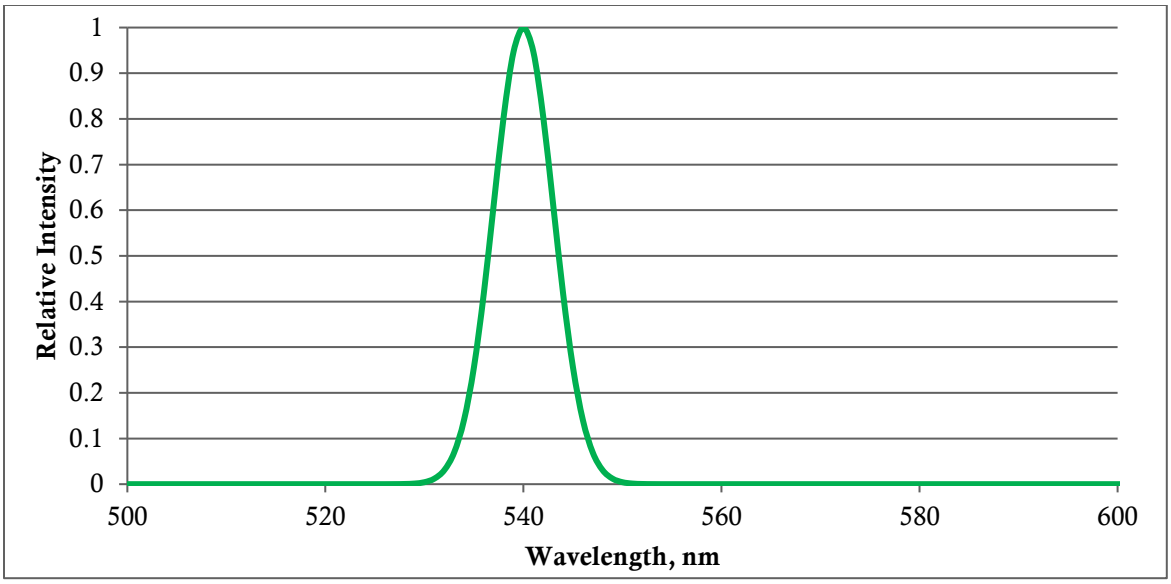

FIGURE 14 - COMPLETE BAND GAP INTENSITY GRAPH FOR HONEYCOMB LATTICE ON UO2, N~2.92, R~0.27

Detecting strain based on the total gap with strain of less than 1% would be very difficult with this small of a wavelength change, while larger changes should be detectable. However, changes in the TM4 gap are considerably greater even at low strain, though the return wavelengths approach UV. The center wavelength with no strain for the TM4 gap is 370 nm. At 1% strain the TM4 gap centers at 359 nm and 5% strain centers at 354 nm. By looking at multiple different return peaks (e.g. TM4, total gap, TM3), it should be possible to detect small changes in strain.

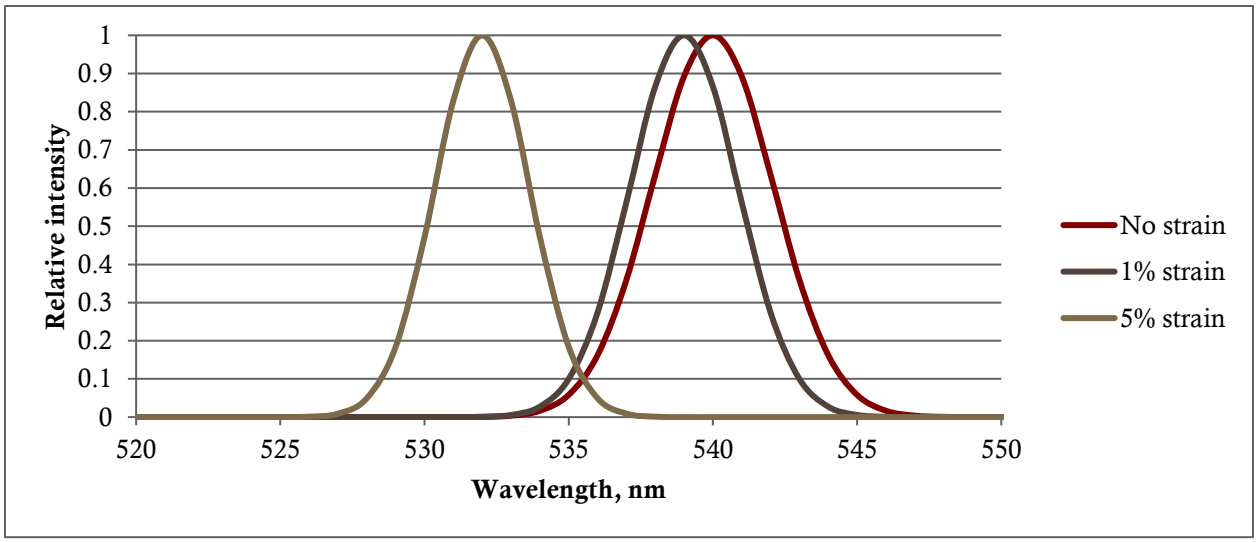

FIGURE 15 - EXPECTED TOTAL GAP RETURN AT VARIOUS STRAINS ON A HONEYCOMB LATTICE, STEEL, R 0.27, N 2.92

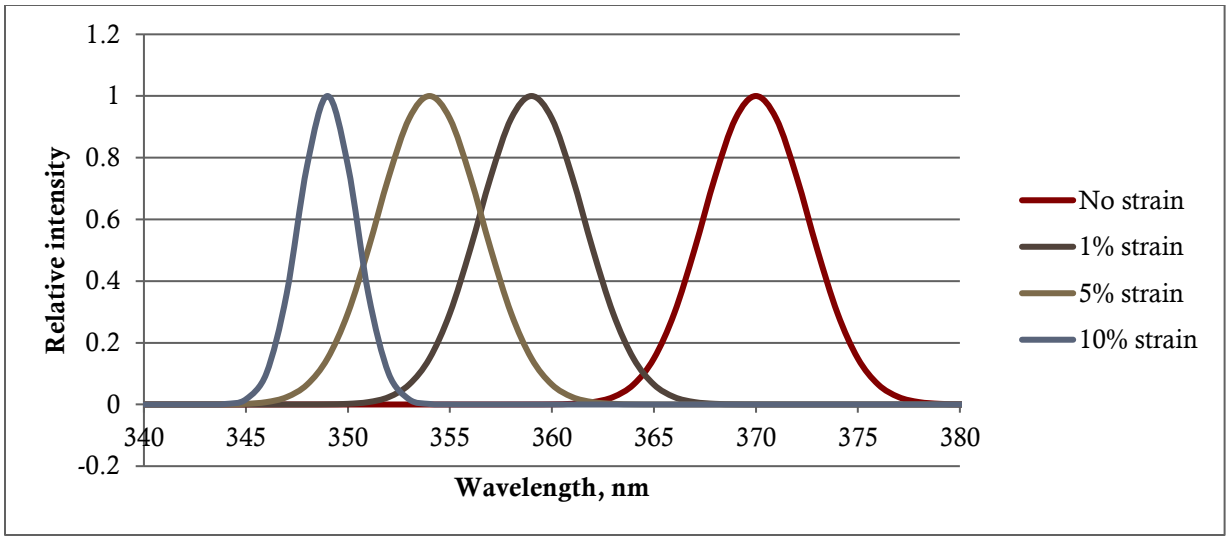

FIGURE 16 - EXPECTED TM4 RETURN AT VARIOUS STRAINS ON A HONEYCOMB LATTICE, STEEL, R 0.27, N 2.92

To simulate the effect of thermal expansion on a photonic crystal, it is necessary to be able to deform the crystal by varying amounts. A square lattice of pillars was simulated, as this is the first lattice structure manufactured. Thermal expansion of a body with a positive coefficient of thermal expansion will cause elongation both laterally and longitudinally. This was simulated by elongating the lattice isotropically while holding the size of the pillars constant.

For the particular square lattice on iron used in these simulations, 2 TE and 2 TM band gaps are present. When un-deformed, the TE1 band gap has a 3.3 nm FWHM and the band gap noticeably shifts from the effects of thermal expansion. Table 3 and Figure 17 show the change in peak wavelength at various strains. Given that the spectro-photometer in use for the NanoVision project is capable of approximately 0.06 nm resolution, small strains should be easily detectable.

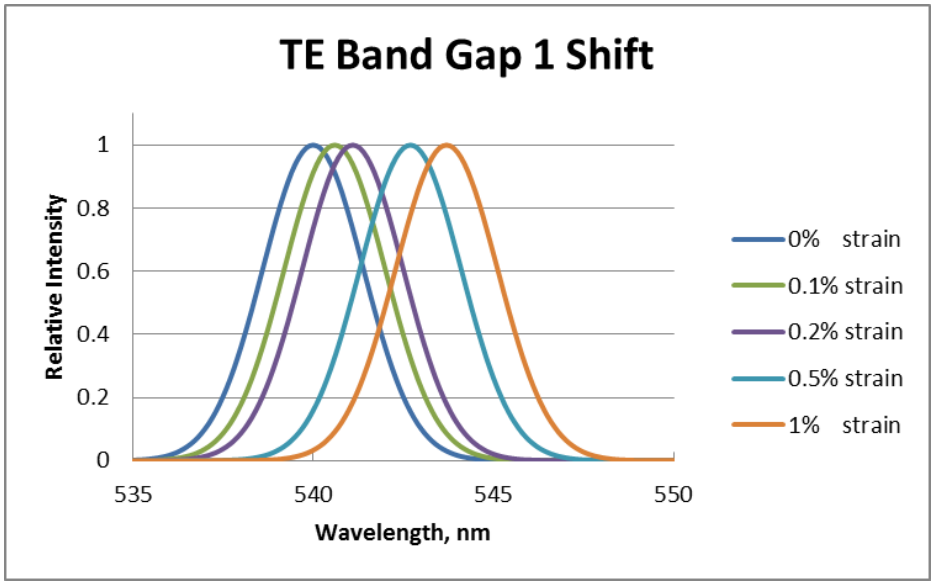

FIGURE 17 - CHANGE IN TE1 BAND GAP WAVELENGTH AS A RESULT OF ISOTROPIC STRAIN (SUCH AS WOULD BE CAUSED BY THERMAL EXPANSION), IN A SQUARE LATTICE OF SQUARE RODS ON STEEL

TABLE 3 - CHANGE IN TE1 BAND GAP CENTER WAVELENGTH IN A SQUARE LATTICE OF SQUARE RODS ON STEEL

Strain	0%	0.10%	0.20%	0.50%	1%
Peak, nm	540	540.3	541.1	542.7	543.7

Additional simulation work has been performed on the subject of photonic crystal behavior under strain. A simple way to model this is to introduce a line defect where the spacing at a single set of columns is increased, as shown in Figure 18.

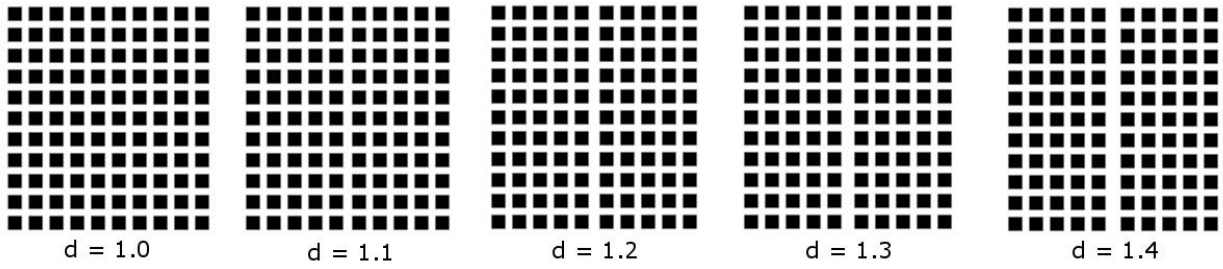

FIGURE 18 - LINE DEFECTS IN A SQUARE LATTICE OF SQUARE RODS

When d=1, there is no defect. A large d means that a single space has been increased by some percentage. A graph showing the simulated outgoing flux of a photonic device with a single line defect of varying dimensions is shown as Figure 19. It is clear upon examination of the results that the change output spectrum is considerably changed by the introduction of a single line defect. Further simulations will be conducted to refine this data and investigate other types of deformation or defects.

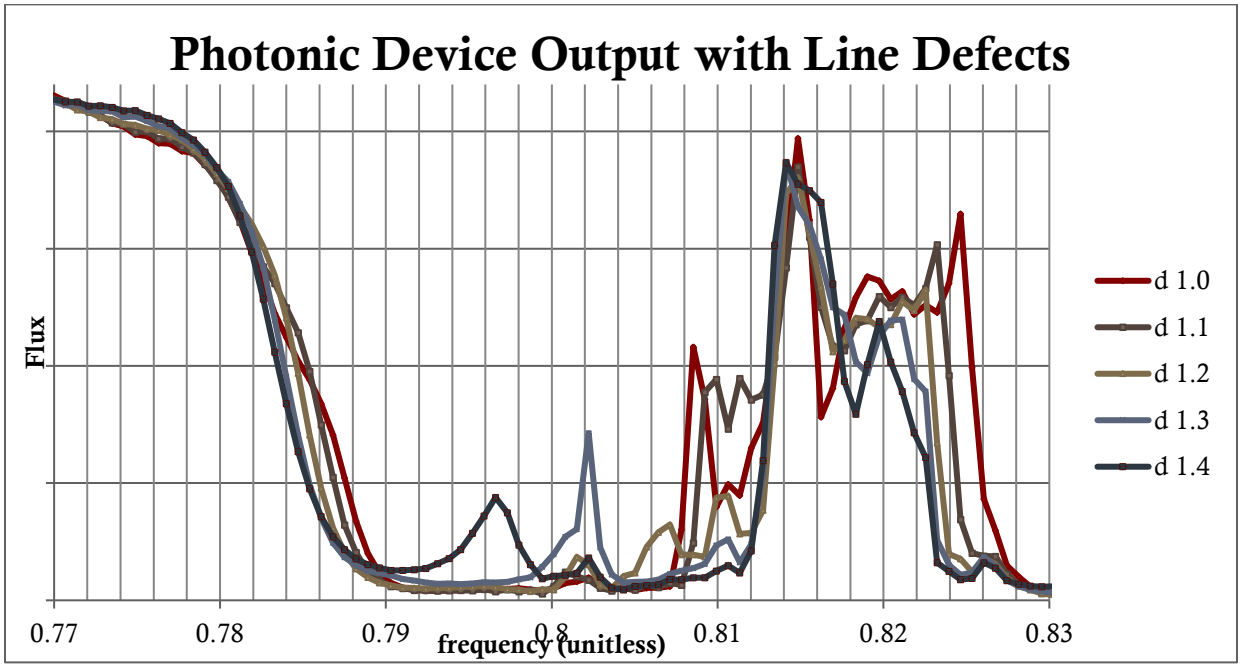

FIGURE 19 - RESULTS FROM LINE DEFECT SIMULATIONS. IF MATERIAL IS ASSUMED TO BE PERFECTLY NON-ABSORBENT, REFLECTION WILL BE THE INVERSE OF THIS GRAPH

FIB Status

Drift issues on the FIB are being addressed with the creation of a custom software package. This package is in the final stages of testing and results are very promising. Autofocus has now been added, and the software is being upgraded for increased reliability and accuracy when performing image matching. These changes will increase the quality of photonic crystal patterns created with this software. Increased accuracy during image matching will be of particular value when attempting to create large continuous crystals. Autofocus should eliminate gradual defocusing of the beam, which leads to poorly defined edges in milled patterns, allowing for longer unattended run times and thus larger photonic crystal arrays.

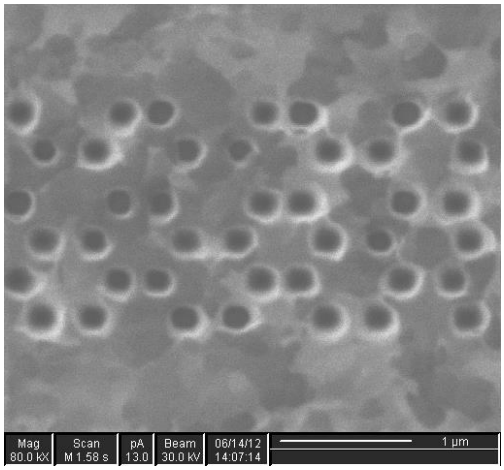

FIGURE 20 - HONEYCOMB LATTICE TEST

Various methods, lattice types and shapes have been experimented with in order to determine optimal milling methodology. At this point, it has been determined that a square lattice of square rods should have a useable band gap and yield the best milling results in the FIB.

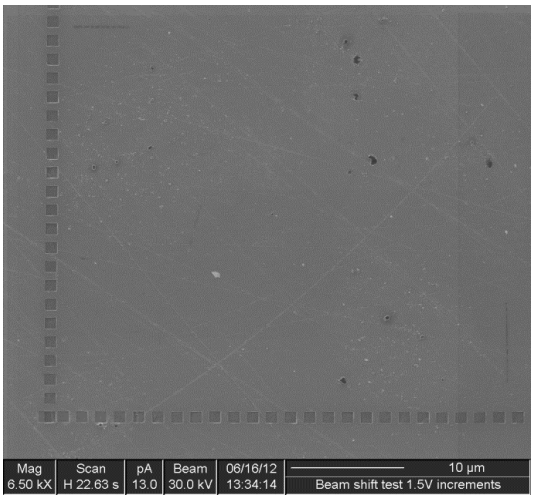

FIGURE 21 - BEAM SHIFT GRID

Focused Ion Beam Milling Experimentation

The FIB tool uses a beam of accelerated gallium ions to image or mill on a sample. This particular FIB has a milling resolution of approximately 4-5nm. The software for this instrument includes a scripting language for the milling of complex shapes; this is particularly useful for large, repeating structures, such as a photonic crystal, because only a single lattice unit need be defined and a loop used to replicate it.

As discussed in previous reports, simulations of photonic crystals in MPB indicated that a honeycomb structure would possess the largest complete (TE and TM polarization) band gap, and so was the first structure selected to attempt. A script was written to mill honeycomb structures with user defined parameters. Initial results with small crystals, on the order of 5-10 microns wide, were promising. However, attempting to move to larger crystals revealed a limit to the number of pattern points inherent in the software that appears to be hard coded or hardware limited.

To work around the pattern point limitation, the microscope's beam shift feature is utilized. It was first necessary to mill a grid of boxes using a fixed voltage beam shift in order to create a relation between beam shift voltage and the resulting shift in SI units. This was easily accomplished and a linear equation fit to the data.

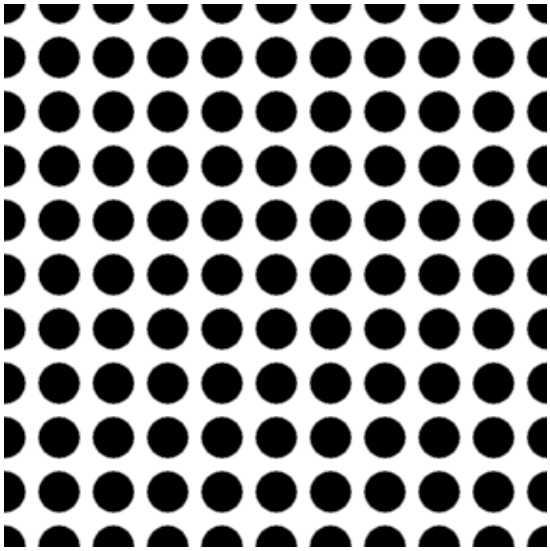

FIGURE 22 - SQUARE LATTICE OF ROUND RODS

With a completed beam shift voltage to microns correlation, scripts were written and run which use beam shift to align multiple smaller patterns to create a single larger crystal. This proved troublesome for honeycomb lattices due to slight drift during milling causing patterns to overlap. In order to alleviate this issue, new calculations were run in MPB to determine if a square lattice of rods would yield useful band gaps. In this case a square lattice of rods did not possess a complete band gap, but does yield a significant TE gap. It was decided that this was acceptable at this stage in the project due to the simplification of fabrication.

Various square lattices were milled and appeared to be yielding promising results. It was at this point that two additional issues made themselves known. First, after attempting to create a large crystal (100 um square) it became clear that the FIB has significant cyclic drift in the x axis. This drift issue needs to be resolved before large continuous crystals can be successfully fabricated.

The second, and more immediately concerning, issue was that upon viewing from a large angle it was clear that the FIB was not producing a lattice of holes as desired. Rather, what was actually produced was more akin to a lattice of roughly pyramidal rods. This is likely due to the fact that in parallel milling mode, which is necessary to prevent backfill of the holes, the beam does not shut off as it moves across the sample. This fact results in the "veins" between holes being milled down significantly and in some places being completely destroyed. It is possible that this issue could be resolved by a high speed beam blanker, but that would also be dependent on how the software is programmed.

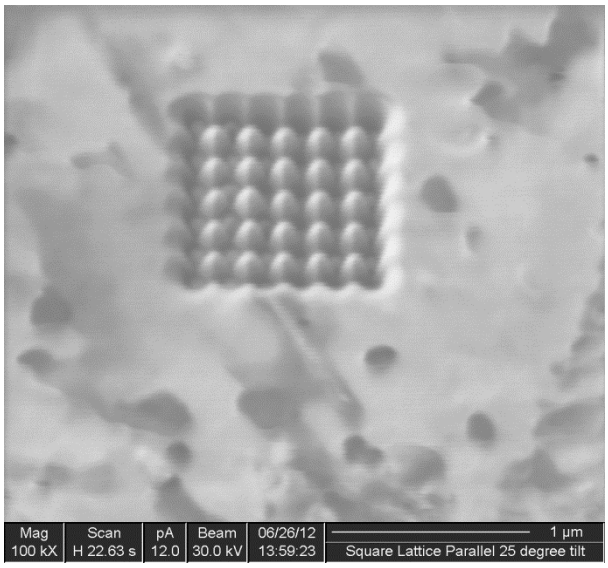

FIGURE 23 - SQUARE LATTICE, 45 DEGREE TILT, NOTE ROD-LIKE STRUCTURE

Instead of attempting to modify the instrument, it was decided to simulate a rod lattice in MPB to determine if such a structure had useable band gaps. When it was found that they did, new milling scripts were written to produce rod lattices. These worked much better than hole lattices, and it is clear from a tilted view that the actual result is fairly close to the desired structure.

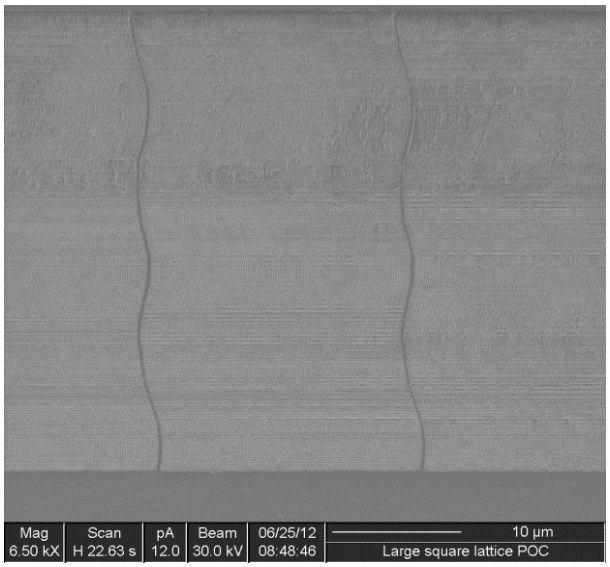

FIGURE 25 - LARGE PATTERN, NOTE CYCLIC DRIFT

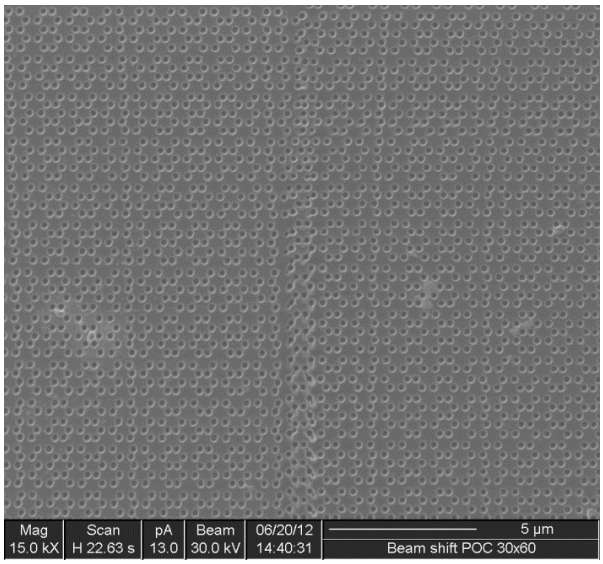

FIGURE 24 - HONEYCOMB LATTICE ON STEEL WITH BEAM SHIFT, NOTE OVERLAP

Experimentation with various methods of achieving a rod lattice led to the consideration of a square lattice of pillars (square "rods"). This structure was simulated in MPB and found to have a sufficient band gap. Fabrication of square pillars in the FIB is considerably simpler than holes or circular rods, and also less time consuming. Both parallel and serial milling methods were attempted with good results, though parallel milling tends to produce shorter rods unless a masking layer is utilized. Serial milling with a re-mill step to alleviate backfill was found to be the most promising method, producing square pillars in steel with good definition in both axes. A cross-section on one of these test patterns was performed in order to observe the depth and aspect ratio of the trenches between pillars.

When drift was sufficiently abated, several additional crystals were milled. Particular emphasis was placed on minimizing milling time. An array of 16 approximately 5um square photonic crystals was produced. Using a 12 pA aperture, this operation has a run time of approximately 17 hours. This is a milling rate of approximately 2.5 minutes per square micron of crystal for this structure, a lattice of square rods. A one millimeter square photonic crystal would be ideal for the micro-tensile samples that have been designed. Unfortunately, a crystal this size would take upwards of 40,000 hours to mill. This is clearly untenable from both a drift and milling time perspective, so alternate manufacturing methods will be pursued for large scale crystals. Smaller crystals, up to approximately 30um on a side, can still be produced on the FIB in approximately 50 hours.

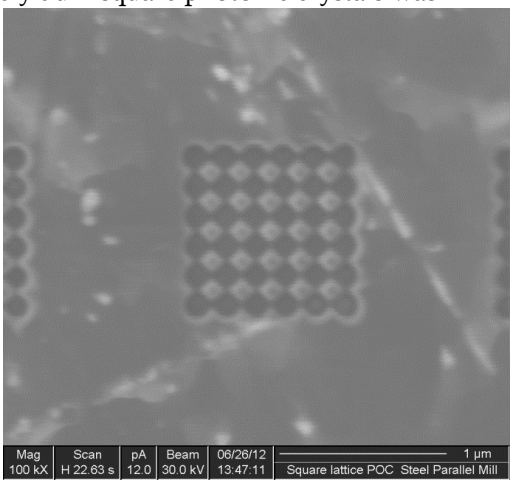

FIGURE 26 - SQUARE LATTICE OF HOLES

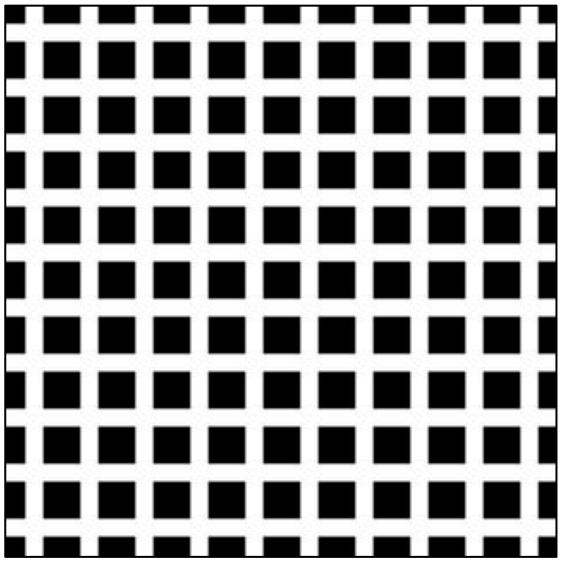

FIGURE 27 - SQUARE LATTICE OF PILLARS, EPSILON MAP FROM MPB

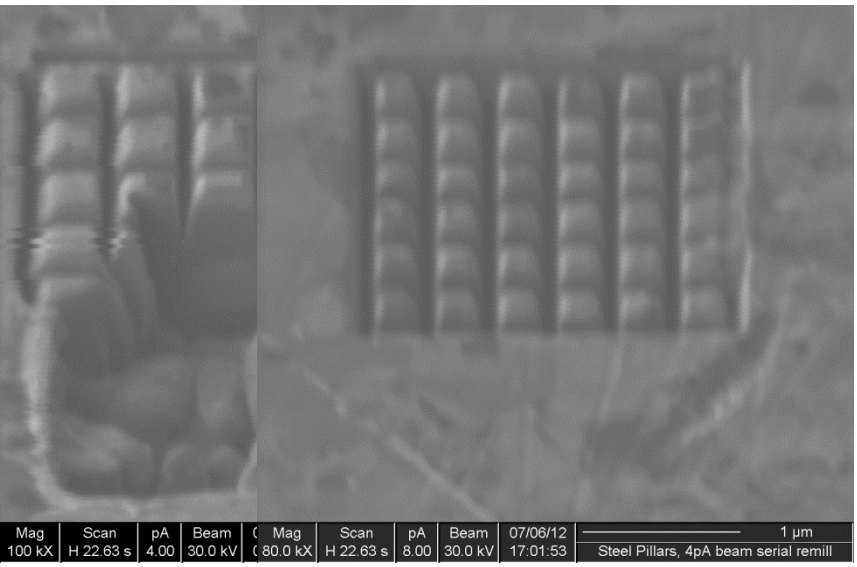

FIGURE 28 - CROSS PILLARS IN STEEL, 4DEGREE TILT

FIGURE 29 - SQUARE PILLARS ON STEEL, 45

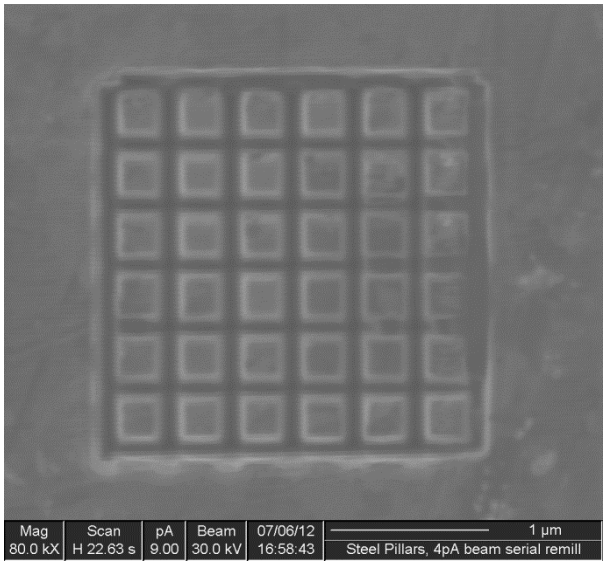

FIGURE 31 - SQUARE PILLARS ON STEEL

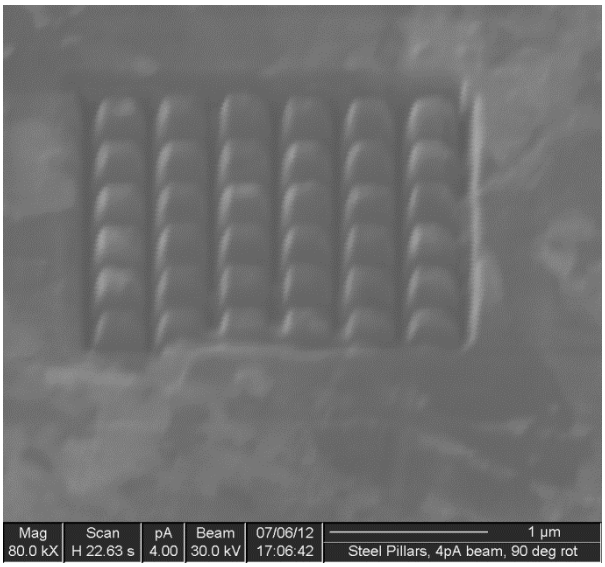

FIGURE 30 - SQUARE PILLARS ON STEEL, 90 DEGREE ROTATION, 45 DEGREE TILT

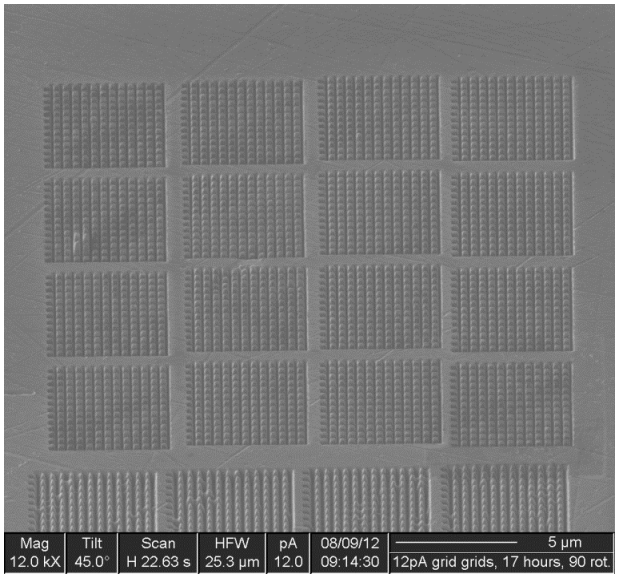

FIGURE 32 - ARRAY OF SQUARE LATTICE CRYSTALS

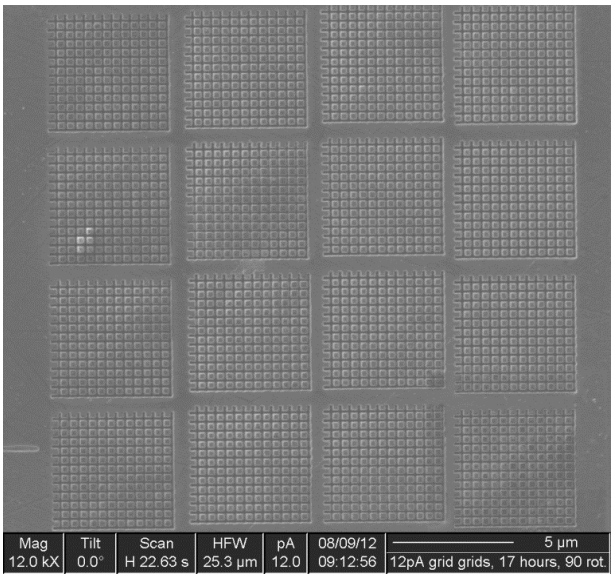

FIGURE 33 - ARRAY OF SQUARE LATTICE CRYSTALS

Verification of Functional Photonic Crystals in Steel

With the completion of a new digital optical microscope system, we have been able to examine previously machined structures at high optical magnification to determine if they are functional as photonic crystals. The system is equipped with a 10 megapixel CMOS camera for recording optical micrographs. The first crystal examined with the new camera was the large array of square rod, square lattice crystals shown in Figure 32 and Figure 33. Figure 34 shows these structures viewed via optical microscope with top lighting. Each individual crystal is approximately 5x5 μm.

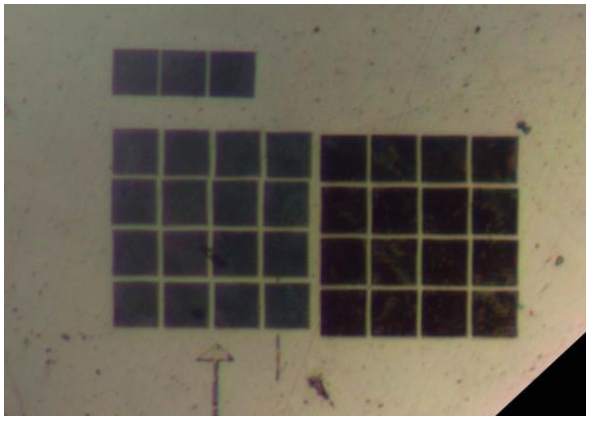

FIGURE 34 - PHOTONIC CRYSTAL ARRAY IN STEEL UNDER DIRECT TOP-LIGHTING

Due to the fact that these photonic crystals are designed on the assumption of light being incident on them perpendicular to the axis of the rods, it is necessary to use side lighting in order to observe any photonic effects. Figure 35, Figure 36 and Figure 37 show the same arrays under varied side-lighting conditions. In these figures the white line represents the location of a line intensity scan broken into the three color channels at right of the image. As the angle of incident light is changed, the returned wavelength from the photonic crystal array also changes. The un-machined surface appears black because the incoming light is at a steep enough angle that it is not reflected into the lens of the microscope. This behavior is confirmation of a functional photonic crystal in steel.

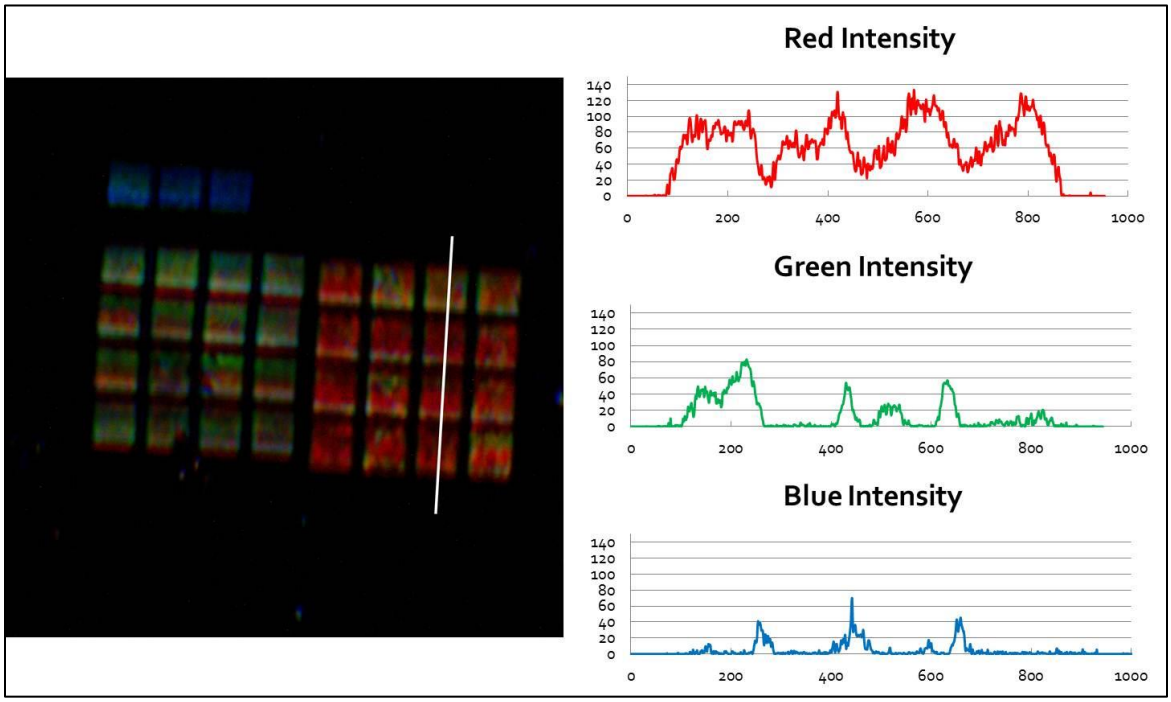

FIGURE 35 - PHOTONIC EFFECT UNDER SIDE LIGHTING OF A CRYSTAL ARRAY IN STEEL

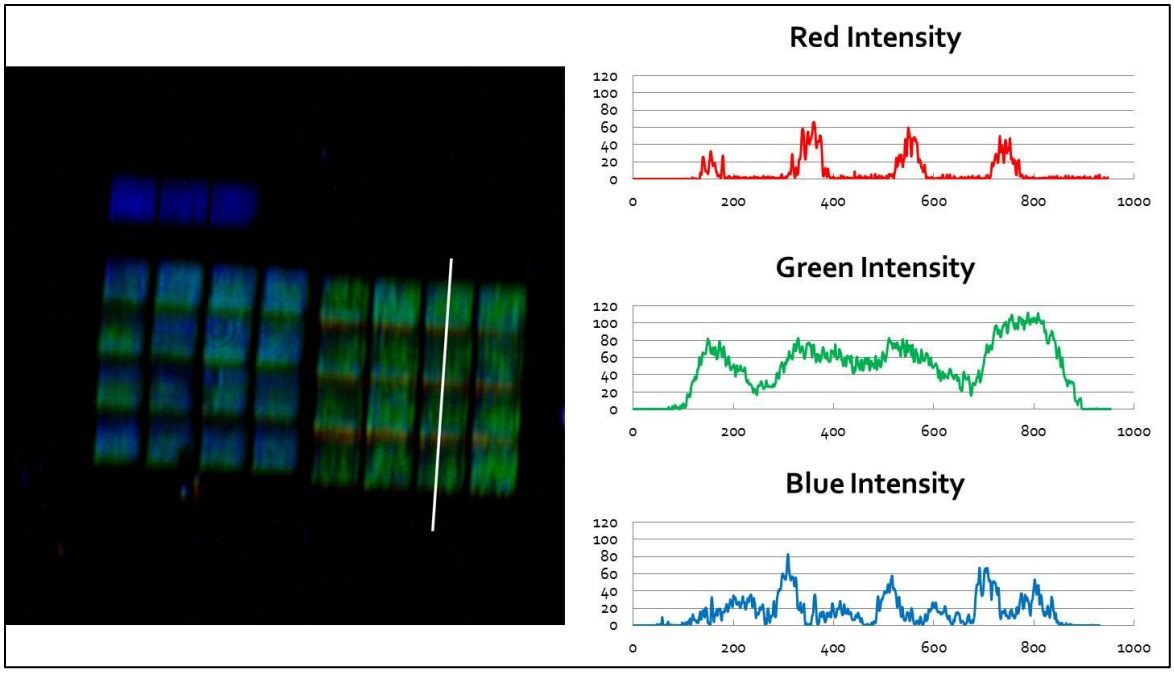

FIGURE 36 - PHOTONIC EFFECT UNDER SIDE LIGHTING OF A CRYSTAL ARRAY IN STEEL

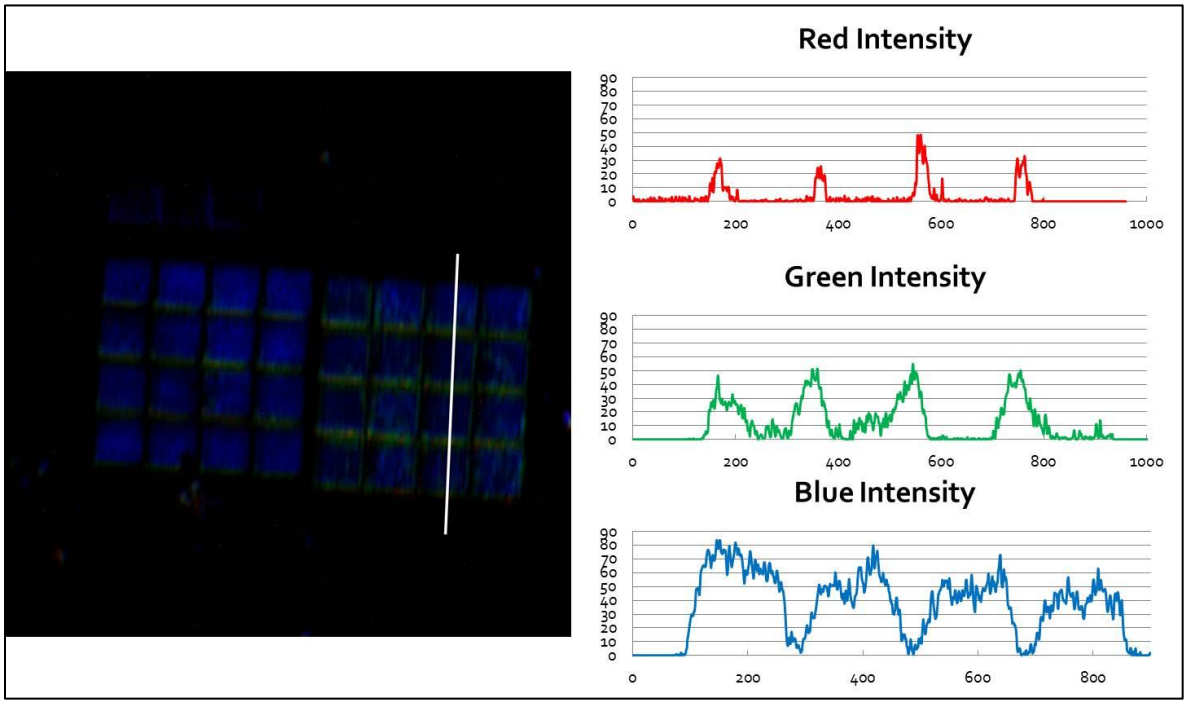

FIGURE 37 - PHOTONIC EFFECT UNDER SIDE LIGHTING OF A CRYSTAL ARRAY IN STEEL

Large Arrays of Photonic Crystals

Continued experimentation with larger beam currents for milling with the DualBeam system showed that photonic effect could be observed in 2-D crystals produced with a 300pA beam. Producing devices at this beam current is sufficiently fast to allow for the production of large arrays of photonic crystals. A 2x2 array of 15x15 arrays of 5um photonic crystals is large enough of be visible without optical magnification.

In order to speed production of photonic devices for basic strain sensors, a Bragg grating (a one dimensional photonic crystal) should be sufficient. Since this requires only a set of parallel lines milled into the material of, these structures can be milled considerably faster and thus be made much larger, than 2-D photonic crystals devices. At present, the FEI DualBeam is capable of producing 150x150um Bragg gratings in steel in approximately 21 hours of milling time. These gratings are large enough to be visible without optical magnification which will open new options for optical interrogation.

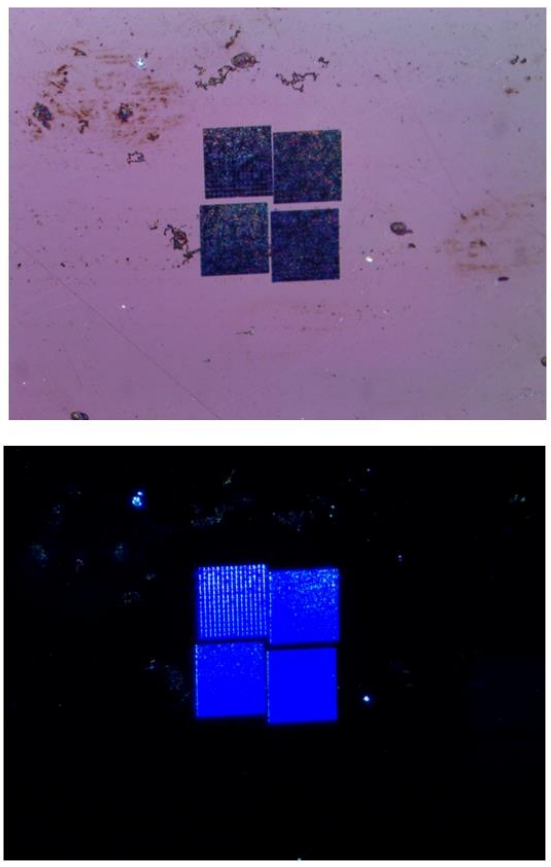

FIGURE 39 - A 2X2 ARRAY OF 15X15 ARRAYS OF 5UM PHOTONIC CRYSTALS

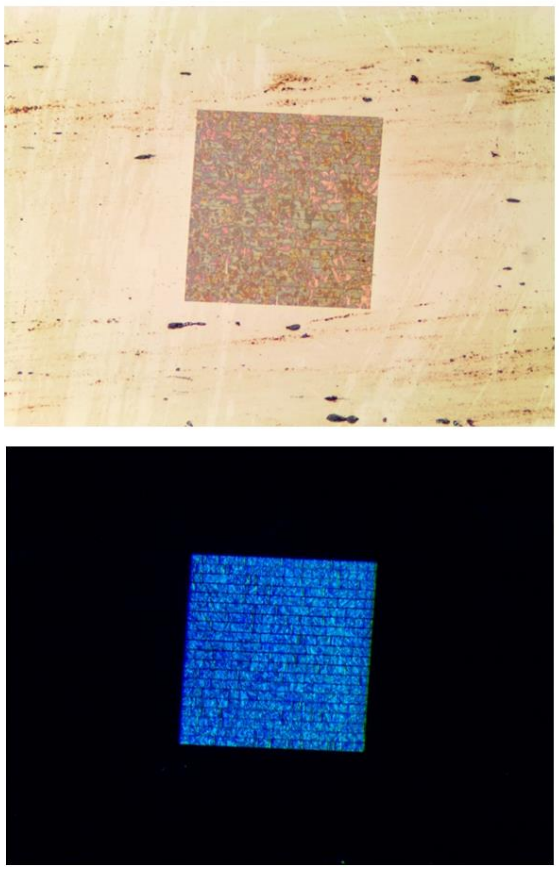

FIGURE 38 - A 150UM SQUARE 1-D PHOTONIC CRYSTAL

Very Large Bragg Gratings

A very large Bragg grating (~150x450um) has been produced for initial proof of concept work on using a Light Gauge sensor as part of a hardness tester. A sensor this large is easily visible to the naked eye.

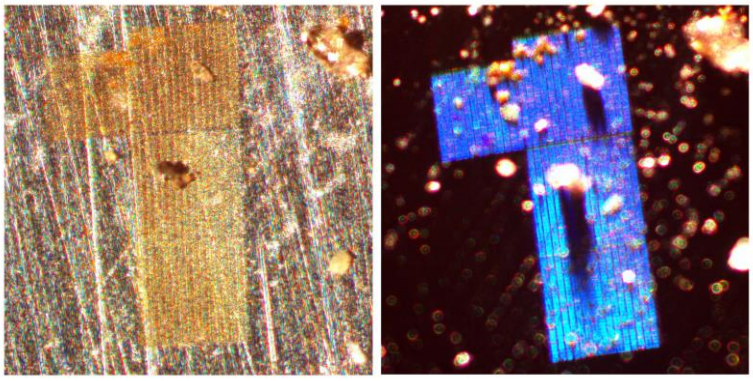

FIGURE 40 - LARGE BRAGG GRATING ON STEEL (~450X150UM). LEFT: TOP LIGHT, RIGHT: SIDE LIGHT

The photonic device was milled onto a long and thin steel strap that is designed to bend as force is applied to the indenter of a hardness tester. The photonic device will deform under bending stress and the change in return wavelength is then correlated to bending strain. From strain, the deflection of the beam and thus the depth of the indentation can then be calculated. Data from a test run is shown below in Figure 41.

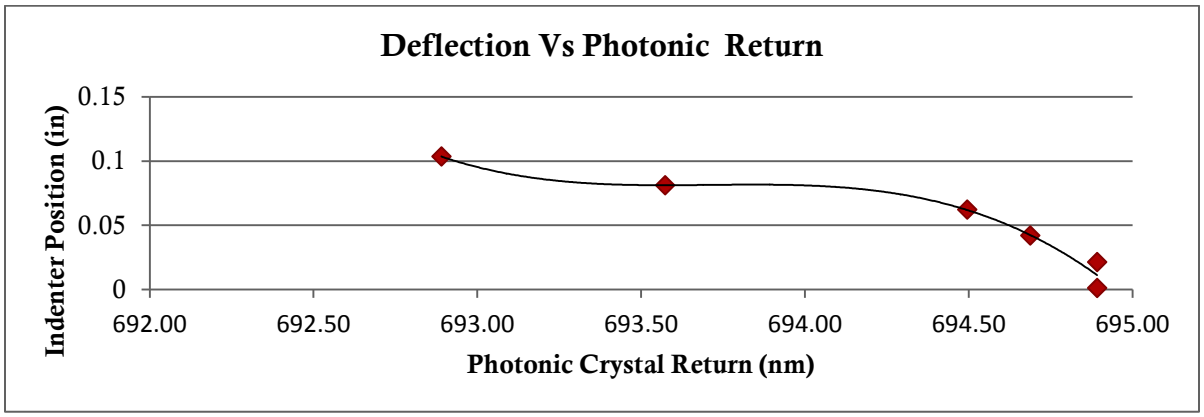

FIGURE 41 - GRAPH SHOWING BRAGG GRATING RETURN VS INDENTER POSITION

This data, while perhaps not ideal, seems to indicate that this concept is feasible. Additional attention to the configuration of the measurement setup is necessary; given the heavy angle dependence observed over the course of measurements on a variety of photonic crystals, it is imperative that the relative position of the light source, photonic device and sensor remains fixed. With the initial measurement rig built to begin testing the LightGauge hardness tester concept, it is likely that the geometry of the sensor, source and photonic device was not sufficiently stable. Specifically, it is suspected that as the strap bent, the photonic device was moving slightly away from the light source, which may have affected the return wavelength.

Spectrophotometer Measurements

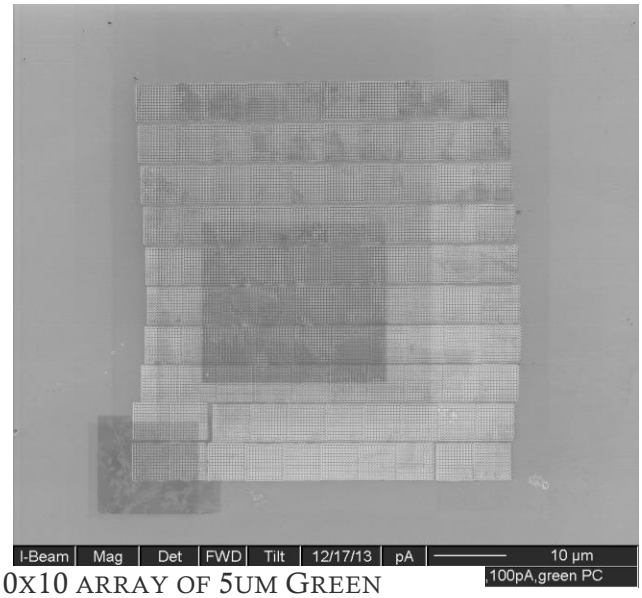

FIGURE 42 - 10X10 ARRAY OF 5UM GREEN OPTIMIZED PCS ON STEEL

A 10x10 array of 5um photonic crystals in steel (shown in Figure 42) was recently produced and subjected to interrogation via spectrophotometer. Side lighting was provided with a halogen bulb, flexible light pipe style microscope illuminator. The incident angle was manipulated to give a strong green return before measurement. Due to the limited wavelength range that the spectrophotometer can measure simultaneously, three different measurements were taken, centered at 420, 540 and 650 nm. Background (blank steel) and photonic device return were measured for each wavelength range and subtracted. The resulting graph is shown in Figure 43.

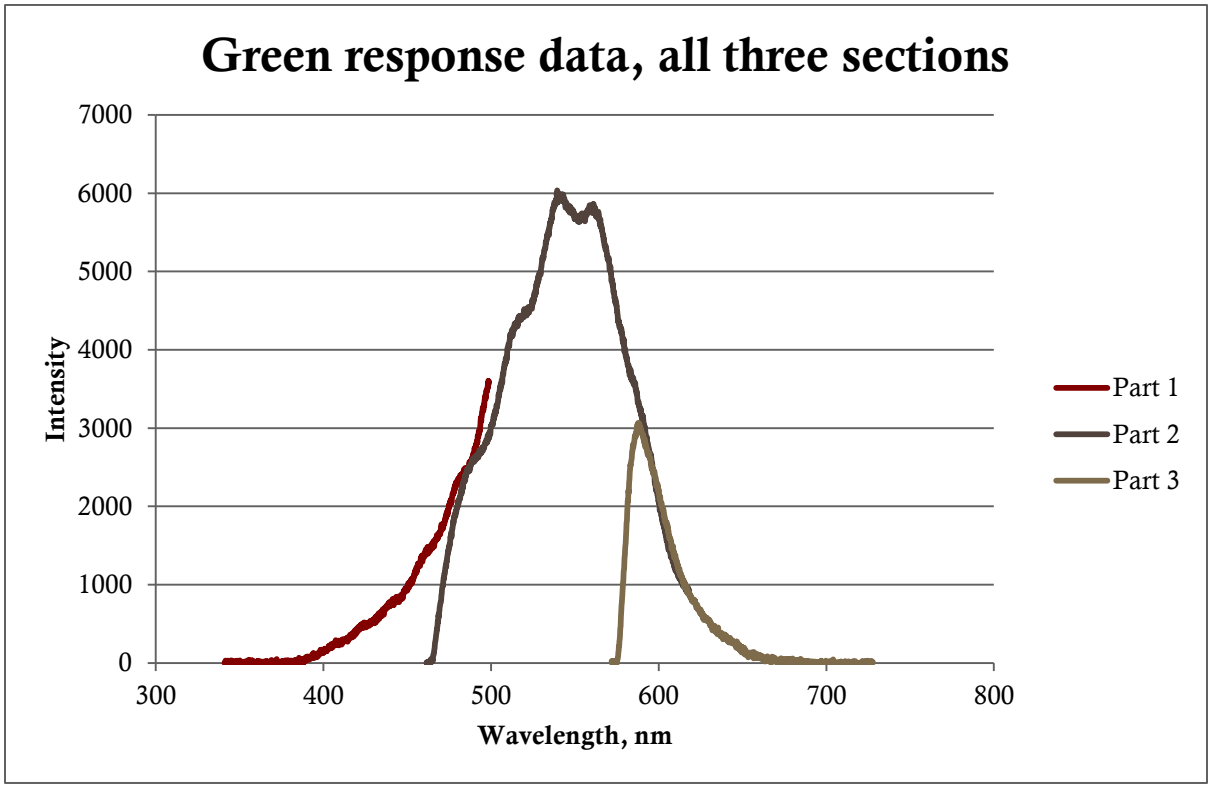

FIGURE 43 - SPECTROPHOTOMETER RESULTS FOR A GREEN OPTIMIZED PC ON STEEL

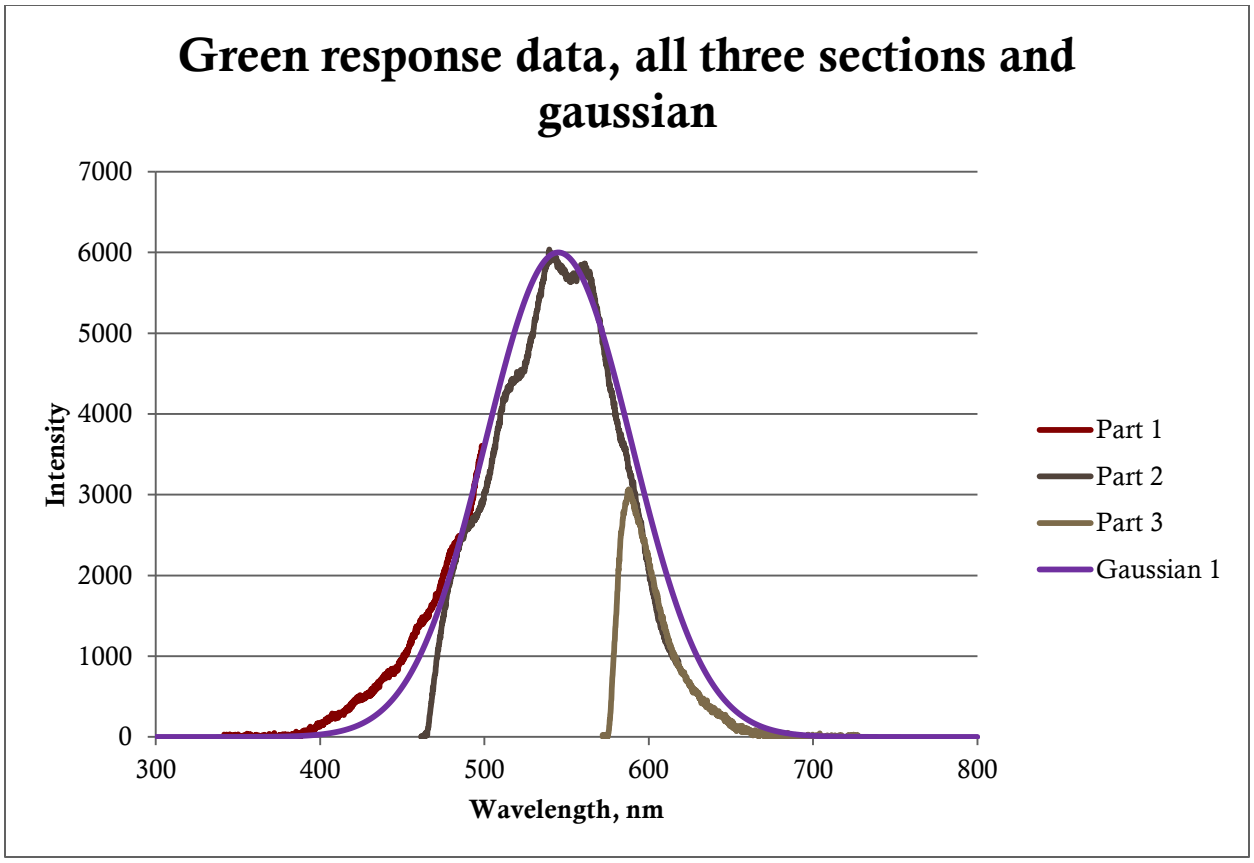

FIGURE 44 - SPECTROPHOTOMETER RESULT FOR A GREEN OPTIMIZED PC ON STEEL PLUS GAUSSIAN APPROXIMATION

Analysis shows that the centroid of the green peak is in the vicinity of 540nm and the full width half maximum of this peak is approximately 100nm. Figure 44 shows the actual data measured plotted against a Gaussian curve with its centroid at 545nm and FWHM of 105nm. Simulations via MPB indicated that a perfect photonic device of this design on pure iron should yield a peak with a centroid at 540nm and a band gap width of approximately 50nm. Accounting for slight changes to refractive index and physical imperfections in the photonic device due to real world production constraints, these measurement results represent promising concurrence with simulation.

Potential New Interrogation Techniques

With the introduction of the 1D photonic crystals for proof of concept which are visible without optical magnification, modified interrogation methods can be considered. Since the return on a Bragg mirror is strongest when the light source and detector are on the same line, a specialized fiber optic bundle has been acquired. This cable is composed of multiple individual fibers. The center fiber is the sensor return, and the outer fibers are the light source. The interrogation end is a single SMA connector, while the light source and sensor fibers are each a separate SMA connector at the other end. This allows for light to be delivered and the return signal examined along the same line, which should give the strongest return with a Bragg mirror.

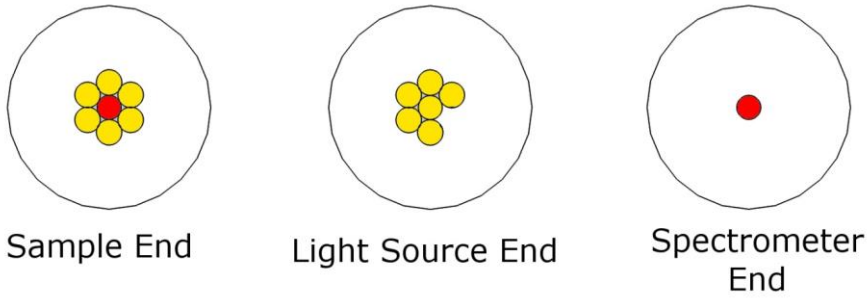

FIGURE 45 - DIAGRAM SHOWING THE THREE ENDS OF A REFLECTION PROBE FIBER. THE SAMPLE END USES A SINGLE FIBER FITTING TO BOTH ILLUMINATE AND MEASURE THE SAMPLE.

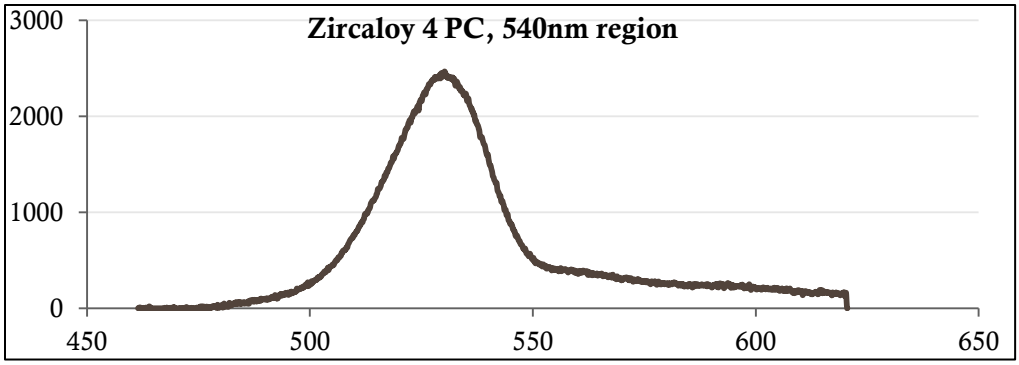

FIGURE 46 - GREEN RETURN FROM A ZIRCALOY-4 PC USING THE SINGLE-BUNDLE INTERROGATION TECHNIQUE. THE PEAK HAS AN APPROXIMATE FWHM OF 11NM, AND AN APPROXIMATE CENTER WAVELENGTH OF 529NM

In addition to the single-bundle interrogation technique, a new stage has recently been acquired which will improve the repeatability and accuracy of two fiber measurements. This device allows for 2 dimensional tilt, x-y translation, z movement, rotation about the z axis and rotation about the y axis. With a small amount of additional modification, this will allow for any combination of angles between the sample, light source and signal collecting fiber.

Photonic Crystals on UO2

With the recent availability of UO2 material produced on-site, experimentation has begun with the production of photonic crystals on UO2. New MPB simulations have been conducted in order to optimize the photonic crystal design. Once again, a square lattice of square rods is being used for ease of machining. With a lattice constant of 400nm and a rod size of 168nm, a crystal has been designed that should have three visible band gaps in the red, green and blue range. All of these bands should be fairly narrow, with a total width ranging from 2 to 13nm. A group of four such 5x5um crystals can be seen in Figure 47.

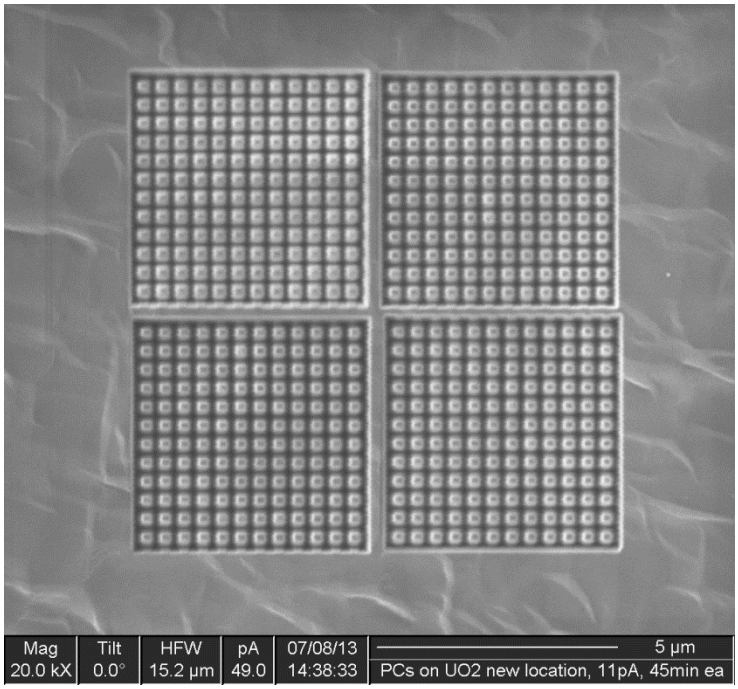

FIGURE 47 - A GROUP OF FOUR 5X5UM PHOTONIC CRYSTALS ON UO2

Below, see the same group of four 5x5um photonic crystals as seen in Figure 46, illuminated under three different lighting angles. These images are paired with histograms of the channel intensities for each image. It is qualitatively quite clear from Figure 46 that functional photonic crystals have been successfully machined onto a UO2 sample.

Photonic Crystals on Zircaloy-4

Zircaloy-4 material has been obtained, simulations conducted and test photonic crystals have been milled on zircaloy. Parameters for zircaloy are somewhat different than steel given its lower real index of refraction, but simulations showed that it should still be possible to produce photonic crystals on this material. An initial test design was created and optimized for bands in the red and blue range. This design was milled using the focused ion beam tool and examined under optical microscopy. Initial results are promising, yielding what appear to be strong red and blue returns, and there remains room for improvement in the quality of the examined crystal. Color micrographs of the zircaloy test photonic crystal are shown below in Figure 49.

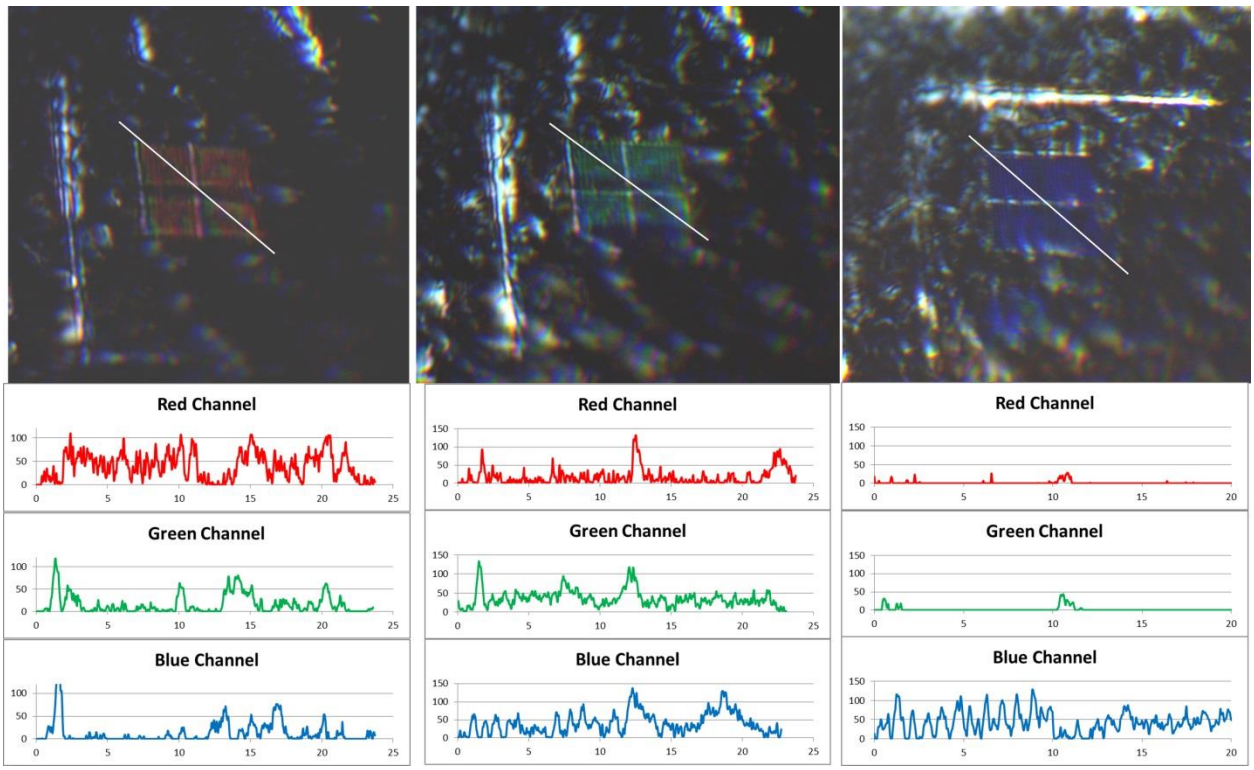

FIGURE 48 - THE SAME GROUP OF FOUR 5X5UM PHOTONIC CRYSTALS AS IN FIGURE 46, ILLUMINATED UNDER THREE DIFFERENT LIGHTING ANGLES, WITH HISTOGRAMS

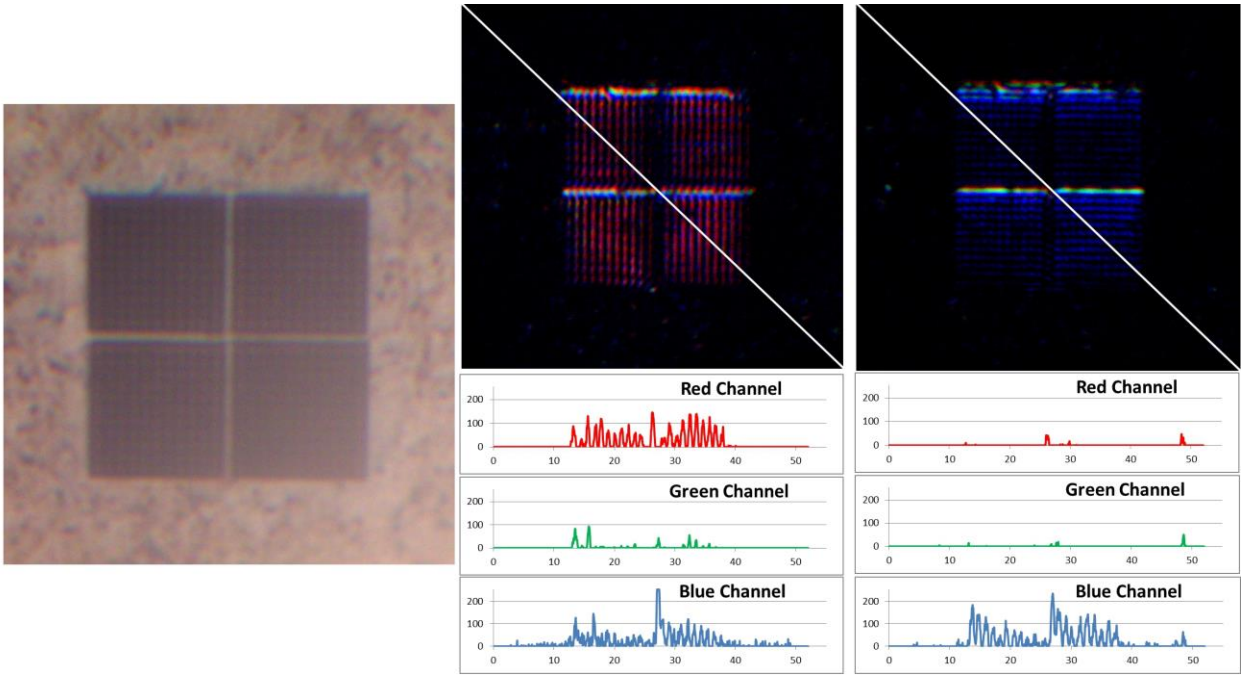

FIGURE 49 - ZIRCALOY-4 PHOTONIC CRYSTAL, OPTICAL MICROSCOPY WITH HISTOGRAMS.

Photonic Structure Fabrication – Moving Forward

The presence of long term drift remains an obstacle to the production of large continuous structures, even with the drift correction software. This is due to the fact that there is no way to pause milling in the middle of a single shape (e.g. one trench) and thus each shape must be small enough to mill at a timescale where drift is not an issue. Another potential work-around is to produce a large number of smaller structures. Provided each structure is large enough to act as a photonic crystal, a large number of smaller structures should yield a return of comparable brightness to a single structure with similar area. This has been carried out in the FIB, and initial optical observation appears promising. The sample has not yet been examined with the spectrophotometer.

Testing has also begun with the goal of determining the minimum depth necessary to produce a functional photonic structure. Initial results indicate that it may be possible to reduce milling depth by as much as a factor of 3, which of course significantly reduces milling time and thus leads to the possibility of producing larger crystals. Figure 50 and Figure 51 depict an early depth reduction test, with top-light and side-light respectively.

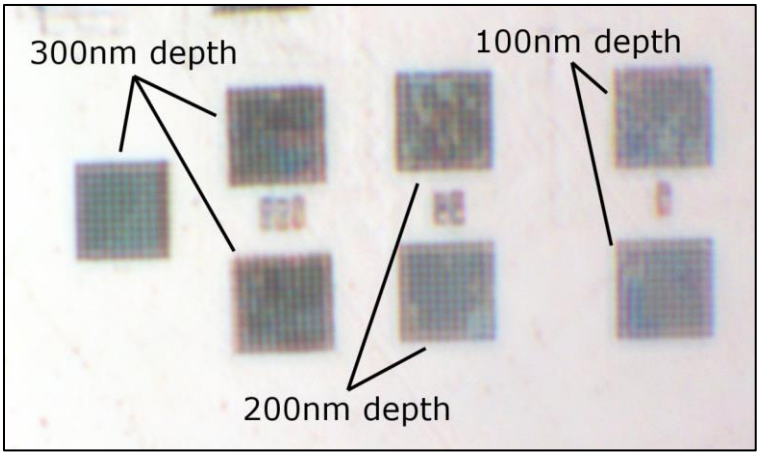

FIGURE 50 - TOP LIGHT OPTICAL MICROGRAPH OF AN EARLY MILLING DEPTH REDUCTION TEST

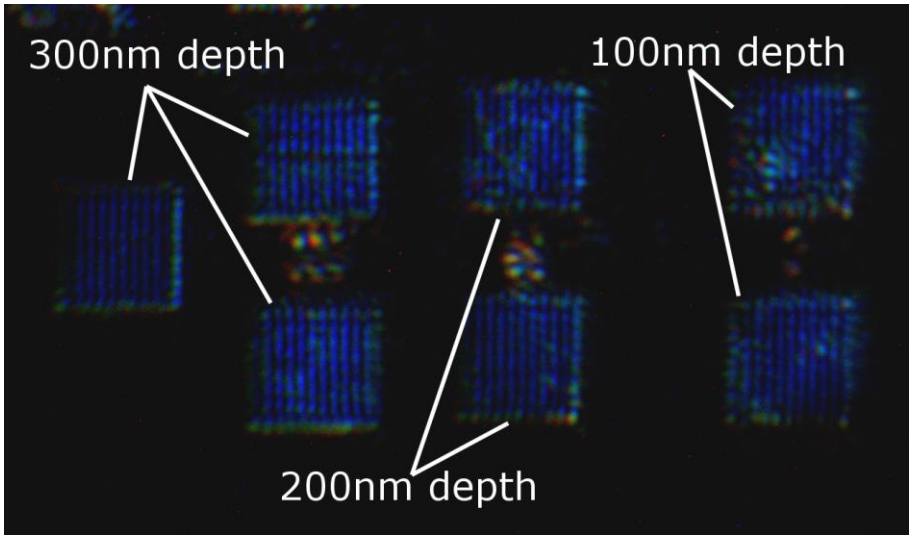

FIGURE 51 - SIDE LIGHT OPTICAL MICROGRAPH OF AN EARLY MILLING DEPTH REDUCTION EXPERIMENT. NOTE THAT THE RETURN ON 300NM AND 100NM CRYSTALS APPEARS SIMILAR

In the longer term, some more advanced techniques are being examined. For instance, the use of a masking layer will significantly alleviate the over-mill problem with parallel milling. This process would involve coating the sample (either entire or in the area to be milled) with a substance that is resistant to the gas used for enhanced etching before the sample is placed in the FIB. The pattern is then milled as normal with the enhanced etch active. The masking layer will resist etching in the vein areas where the beam dwell time is shorter. Where the beam dwell time is longer (holes) the mask will be burned through and the material below quickly etched. A simpler form of this concept was employed

with success using platinum over silicon – the platinum layer was fully removed across the full pattern, and the silicon rods below were significantly taller than those generated by a similar parallel etch without a platinum layer. A carbon sputter-coating is being considered for this purpose and also to cut down on reflection from the un-milled surfaces of polished samples. Reducing or eliminating simple reflection will improve the effectiveness of the spectrophotometer during testing.

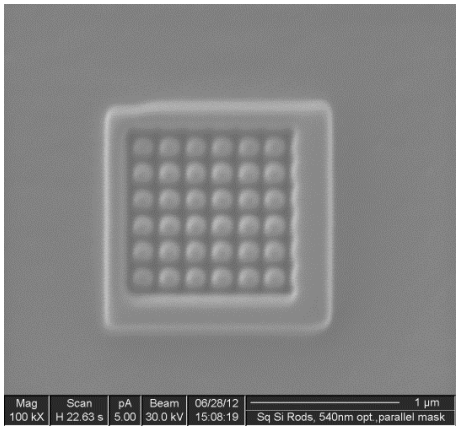

FIGURE 52 - RODS IN SILICON THROUGH PLATINUM MASK

There are additional possibilities for crystal fabrication that would utilize the FIB to deposit or edit a resist layer for subsequent etching in another device, such as a reactive ion etcher; this could be done with a positive or negative resist. Some form of more advanced fabrication method will need to be used in order to successfully create lattices of holes at the appropriate scale to create photonic structures which act in the visible wavelength, since serial milling leads to back-fill and parallel milling to over-mill. It is also now quite clear that an alternate production method will be necessary for the production of large crystals or the large-scale production of smaller crystals.

One alternate production possibility is to utilize processes common in the semi-conductor industry, such as spin-coating, mask layers and reactive ion etching (RIE). An RIE will be necessary (as opposed to, for example, a chemical etch) due to its high degree of anisotropy, since NanoVision crystals require deep and narrow holes or trenches (high aspect ratio). A potential example process is detailed below.

First, a substrate such as steel or silicon is coated with a thick layer of an inexpensive masking material. Another very thin layer of a second mask material is then applied. The upper mask layer is then etched in the appropriate pattern. Given the very small feature size of a NanoVision crystal, this operation will likely be carried out in the FIB, as most lasers would have too large of a spot size. An RIE tool is then used to selectively etch through the upper mask to pattern the lower masking material. A second RIE, of different chemistry, then etches the substrate through the lower mask.

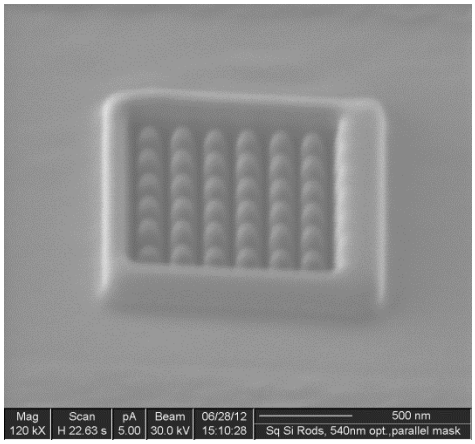

FIGURE 53 - RODS IN SILICON THROUGH PLATINUM MASK, 45 DEGREE TILT

To further expedite the production process, the possibility of some kind of stamping process is also being considered. This would entail a master stamp created with the FIB and used to pattern a mask layer in some fashion. This could potentially allow for large and/or unusually shaped patterns to be created by repeatedly using a single relatively small master stamp to create a large mask prior to RIE etching.

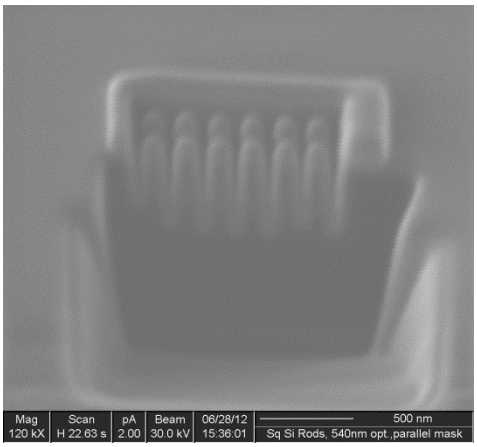

FIGURE 54 - CROSS SECTION OF RODS IN SILICON THROUGH PLATINUM MASK, 45 DEGREE TILT

Deliverable #5 Document reporting the calibration data for the first NanoVision devices.

Milestone #5: Develop calibration data for NanoVision.

Deliverable #5: (Participants) ISU

Deliverable #5: (Status)

Custom Tensile Tester Design

FIGURE 55 - PHIDGET BOARD

The equipment and materials to construct the custom tensile tester and measure stress and strain have been purchased. The custom tensile tester has been built and custom software for recording data measurement has started. The design of the custom tensile tester was modified for the specific equipment purchased and several small changes were made to improve the design. Equipment purchased included the hydraulic ram, strain gages, a load cell and a Phidgets PhidgetBridge Wheatstone Bridge Sensor Interface.

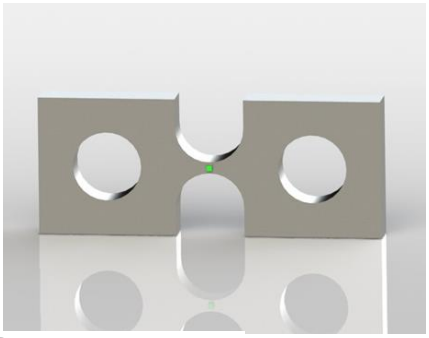

FIGURE 56 - DOG BONE MICRO-TENSILE SAMPLE

Previously NanoVision dog bone micro-tensile samples were designed with a gauge width of 1mm. The micro-tensile samples were designed in this manner to insure that the maximum stress occurs where the photonic crystal will be located. Additionally, a small cross-sectional area insures that the sample will have a low ultimate tensile (breaking) strength, which helps simplify the design of the testing rig.

The gauge width on the micro-tensile samples was modified from 1.2mm to 1.5mm in order to fit the width of the strain gage. The small size of the strain gauge is necessary in order to measure the strain in the reduced cross-section gauge length area of the tensile sample. Appropriately sized strain gages have been purchased to measure the strain on the sample. This strain data will be correlated with the wavelength returned from the photonic crystal in order to develop a wavelength response vs. strain relation. If the strain and cross-section of the sample are known the stress can be calculated using Hooke's Law.

The strain gage will be used in a Wheatstone bridge circuit and the output voltage will be measured using a Phidgets PhidgetBridge Wheatstone Bridge Sensor Interface. This device allows up to 4 un-amplified Wheatstone bridges to be connected and has differential voltage resolution of 24 bits per channel. The differential voltage will be recorded on a computer using a custom software package.

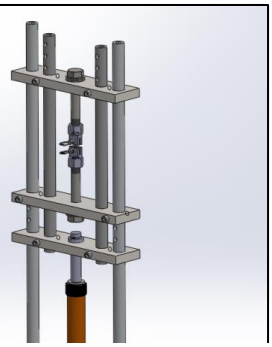

FIGURE 57 - CUSTOM TENSILE TESTER

The custom tensile tester has been built using the equipment and materials previously purchased. Further design work has been carried out for a multi-axis stand to allow for the micro-tensile test rig to be used in conjunction with a high-power optical microscope. This is necessary in order to make it possible to measure the return wavelength of smaller (minimum approximately 20x20 microns) photonic crystals under stress.

Work continues on the production of a DAQ system for the micro-tensile tester. A Raspberry Pi unit is utilized as the modular core of the system, with various add-on boards attached as required. One of these boards is an ADC (analog to digital converter) used to digitize the analog signal from the load cell and any other sensors that may later be added. Using this equipment and various known weights, the calibration of the load cell was confirmed from 0 to 200 lbs. The load cell results were plotted against the known weights, as shown in Figure 588.

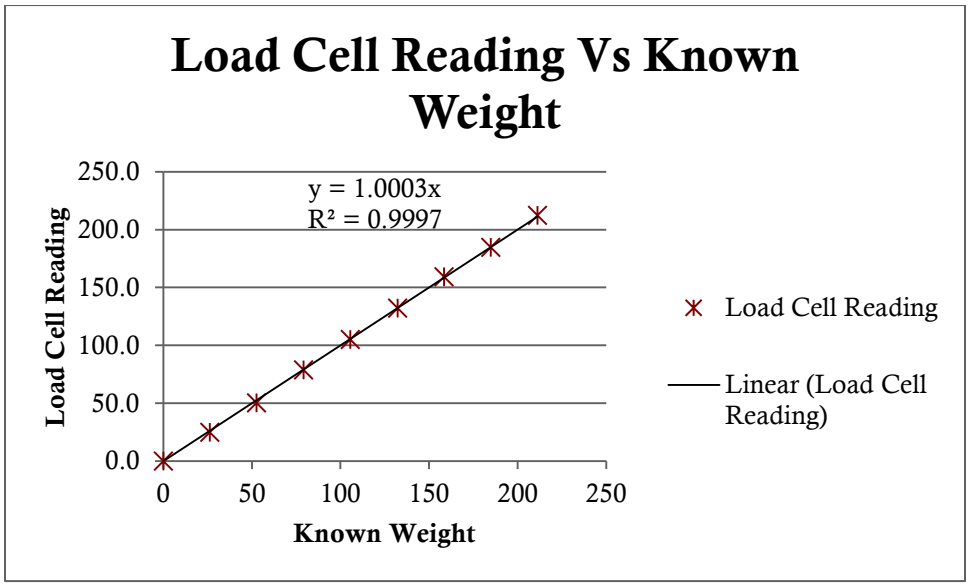

FIGURE 58 - LOAD CELL CALIBRATION TEST

Verification of Sensor Systems on Micro-Tensile

A HBM LY11-0.3/120 strain gage with a temperature response matched for steel was attached to a micro-tensile sample. The sample was then placed in the tensile tester and force applied. Strain and force

were measured in real time. Since the cross-section of the sample is known, force was converted to stress and plotted versus strain, as can be seen in Figure 599.

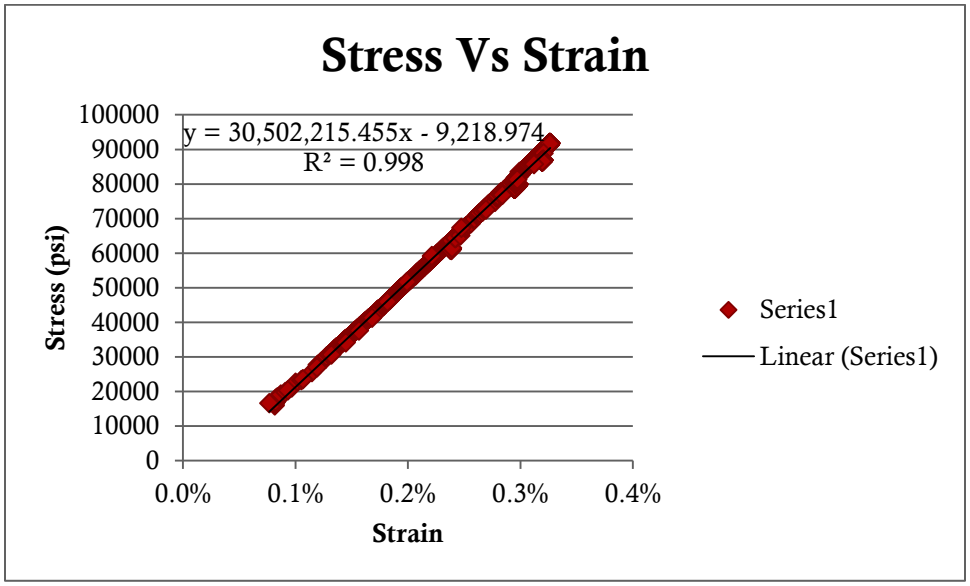

FIGURE 59 - STRESS STRAIN CURVE FOR STEEL MICRO-TENSILE SAMPLE

A linear curve fit of the stress strain data was performed. The slope of this line should be equal to the modulus of elasticity of the steel sample. The modulus of elasticity for steel is typically between 29000 and 30000 ksi. The calculated value was 30.5 ksi, which shows good agreement with theory, thus proving that the measurement system for the micro-tensile tester appears to be functioning as intended.

Deliverable #6 Document reporting the first radiation tests developed.

Milestone #6: Test first fuel materials in radiation field.

Deliverable #6: (Participants) ISU

Deliverable #6: (Status) The first round of neutron and gamma irradiations has been completed.

Post-Irradiation Examination

A post-irradiation sample bearing a 4x4 array of 5um photonic crystals was received and analyzed via focused ion beam and scanning electron microscopy. The presence of gross mechanical damage, likely incurred during shipping, has made it difficult to determine the extent of damage caused by radiation. However, given the apparent high degree of error tolerance observed previously during this project, it appears that the crystals away from the larger scratches will likely still exhibit photonic effects.

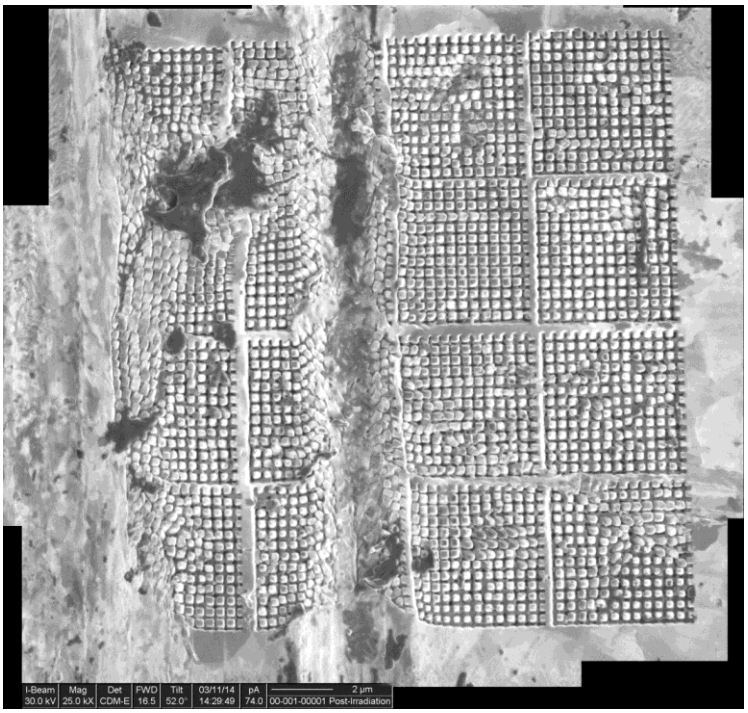

Unfortunately, due to the presence of large scratches over and near the photonic crystal, optical interrogation of this post-irradiation sample has been made unusually difficult. Scratches of this size have faces larger than some wavelengths of light which allows them to act as reflectors. Since one of these scratches runs directly through the photonic crystal, any angle where the light is reflected from part of the scratch into the lens of the microscope cannot be properly analyzed. Optical micrographs of the crystal show a weak blue-green return still visible despite the mechanical damage.

FIGURE 60 - HIGH RESOLUTION FIB MOSAIC IMAGE OF POST-IRRADIATION PHOTONIC CRYSTAL ON STEEL. GROSS MECHANICAL DAMAGE IS READILY APPARENT

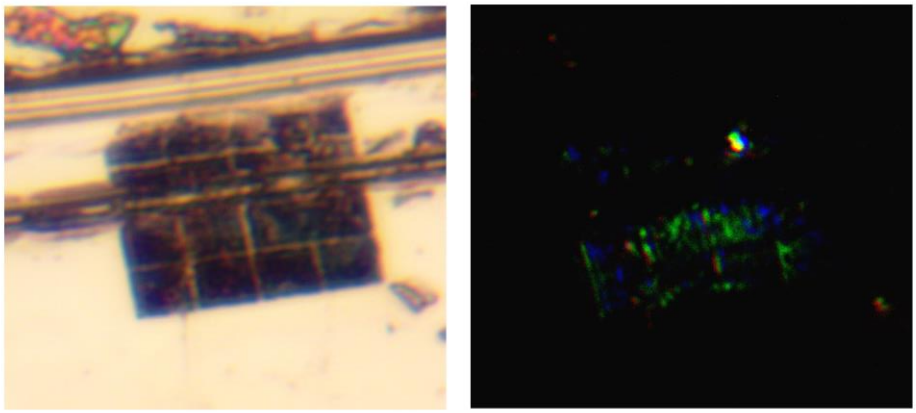

FIGURE 61 - OPTICAL MICROGRAPH OF POST-IRRADIATION PC. TOP LIGHT AT LEFT, SIDE LIGHT AT RIGHT

Deliverable #7 : Document reporting the first fuel based radiation tests developed.

Milestone #7: Test first fuel materials in radiation field
Deliverable #7: (Participants)

Deliverable #7: (Status) These tests are being set up at the time of writing of this report.

Deliverable #8 : Document reporting the performance of calibrated versions of NanoVision developed.

Milestone #8: Calibrate NanoVision's performance on surrogate materials in a radiation field.
Deliverable #8: (Participants)

Deliverable #8: (Status) First tests were completed on a calibrated sensor and the document will be created in the next quarter.

Deliverable #9 : Document reporting the performance of calibrated versions of NanoVision on fuel developed.

Milestone #9: Calibrate NanoVision's performance on fuel materials in radiation field.
Deliverable #9: (Participants)

Deliverable #9: (Status) Will be started following first successful tests.

Deliverable #10 : Final Report.

Milestone #10: Final Report.
Deliverable #10: (Participants)

Deliverable #10: (Status) This is the final report

Deliverable #11 : Quarterly Reports.

Milestone #11: Quarterly Reports submitted.
Deliverable #11: (Participants)

Deliverable #11: (Status) Complete.

Deliverable #12 : Yearly Reports.

Milestone #12: Yearly Reports submitted.
Deliverable #12: (Participants)

Deliverable #12: (Status) Quarterly reports filed.

Deliverable #13 : Consult with outside industry partners for commercialization.

Milestone #13: Several industry partners were consulted and favorable results were obtained. Additional in-core testing would be required for adoption in industry.
Deliverable #13: (Participants)

Deliverable #13: (Status) Have begun demonstrations with commercial entities.

Conclusions

The project has concluded. A new type of sensor was developed and tested with a large degree of success. Probes were irradiated and tested and showed a solid response. The probes can stand up to high DPA doses from proton irradiation and still survive. A full account of this can be found in the thesis by Slavica Grdanovska, Ph.D.

Students

Students currently funded to date at ISU are:

Brycen Wendt, Dallin Steele, Daniel Issacs, Scott McBeath, Slavica Grdanovska.

Budget Data

Project is complete. Funds have been fully spent.

References:

1. http://www.luxpop.com/.
2. P. B. Johnson and R. W. Christy, "Optical constants of transition metals: Ti, V, Cr, Mn, Fe, Co, Ni, and Pd,"*Phys. Rev. B*, Vol. 9, No. 12, 15 June 1974, pp. 5056-5070.
3. Joannopoulos et. al., *Photonic Crystals: Molding the Flow of Light*, Princeton University Press, New Jersey, 2008

Appendix A – Additional Intensity Graphs

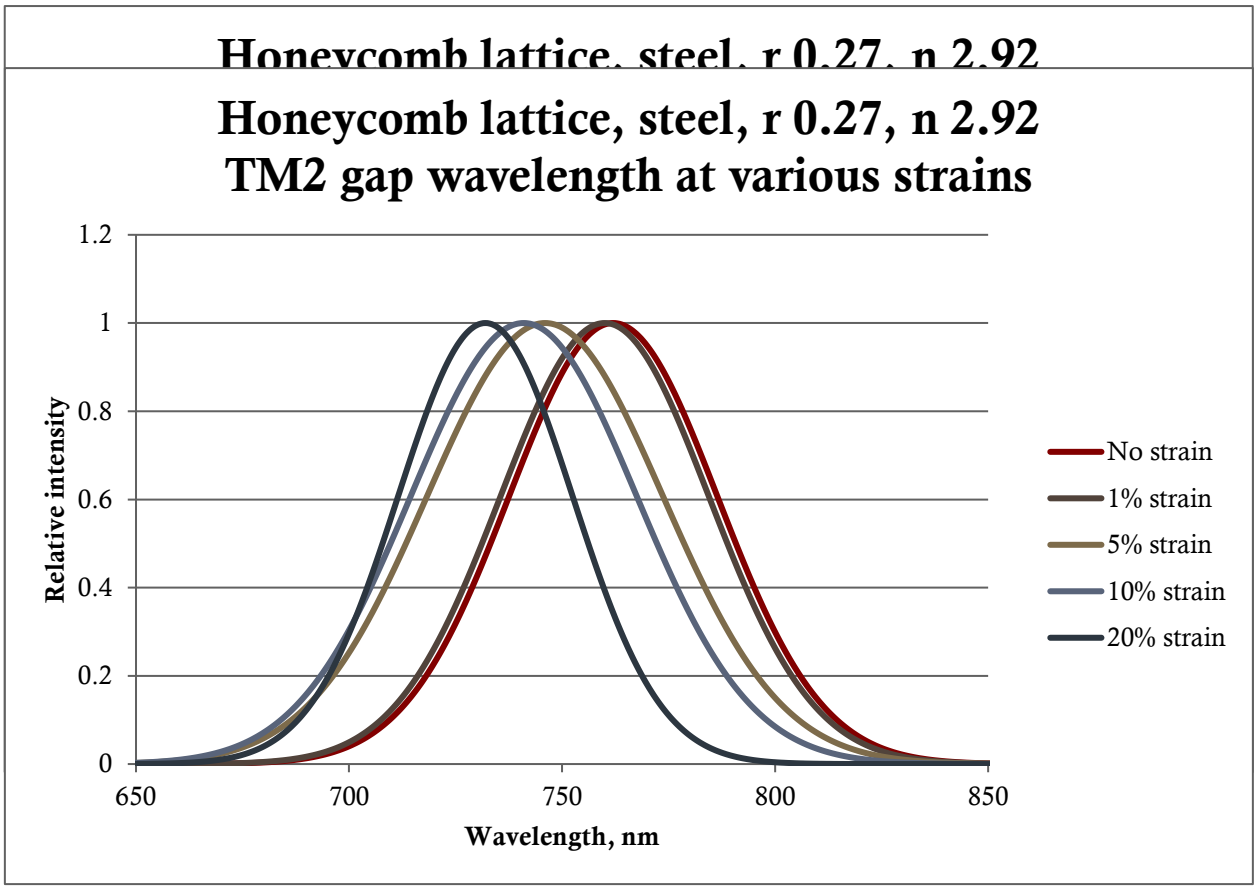

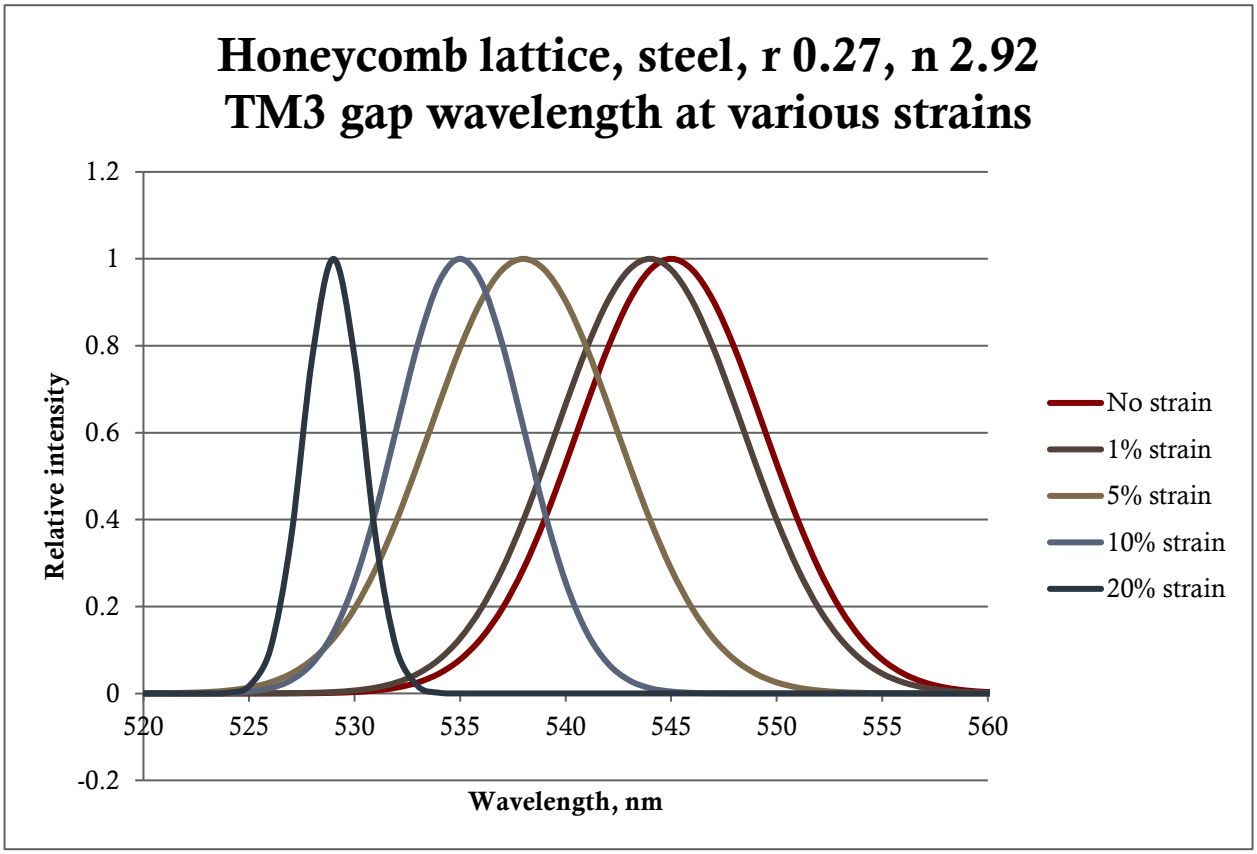
Honeycomb lattice, steel, r 0.27, n 2.92
TM3 gap wavelength at various strains
Relative intensity
1.2
1
0.8
0.6
0.4
0.2
0
-0.2
520
525
530
535
540
545
550
555
560
Wavelength, nm
No strain
1% strain
5% strain
10% strain
20% strain

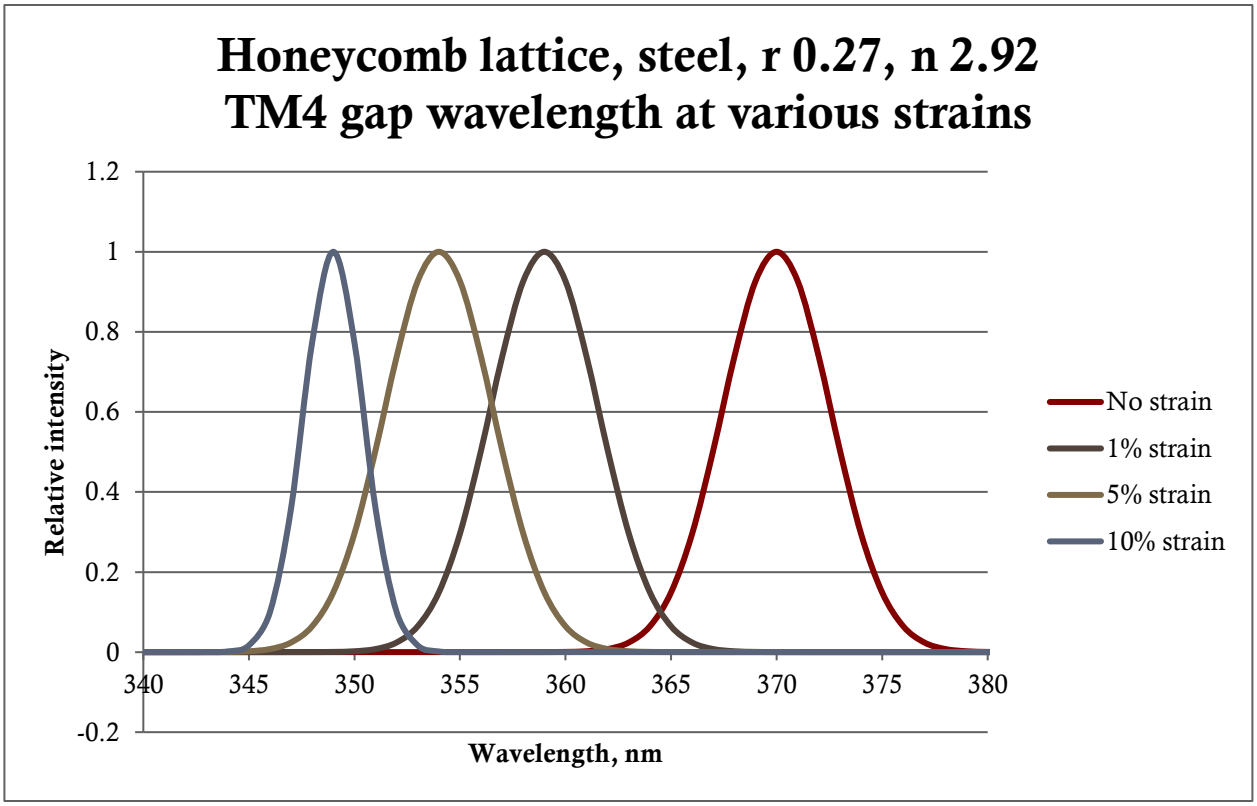
Honeycomb lattice, steel, r 0.27, n 2.92
TM4 gap wavelength at various strains
Relative intensity
1.2
1
0.8
0.6
0.4
0.2
0
-0.2
340
345
350
355
360
365
370
375
380
Wavelength, nm
No strain
1% strain
5% strain
10% strain

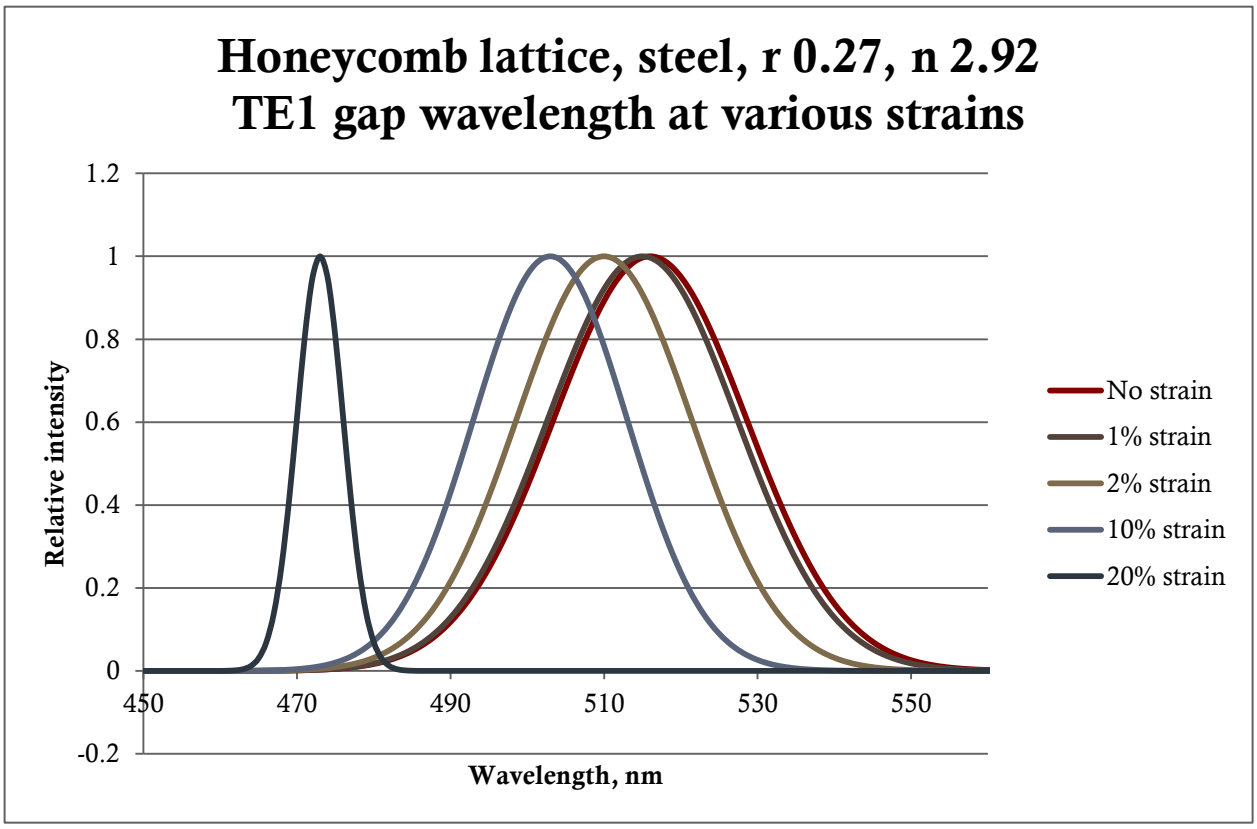
Honeycomb lattice, steel, r 0.27, n 2.92
TE1 gap wavelength at various strains
Relative intensity
1.2
1
0.8
0.6
0.4
0.2
0
-0.2
450
470
490
510
530
550
Wavelength, nm
No strain
1% strain
2% strain
10% strain
20% strain

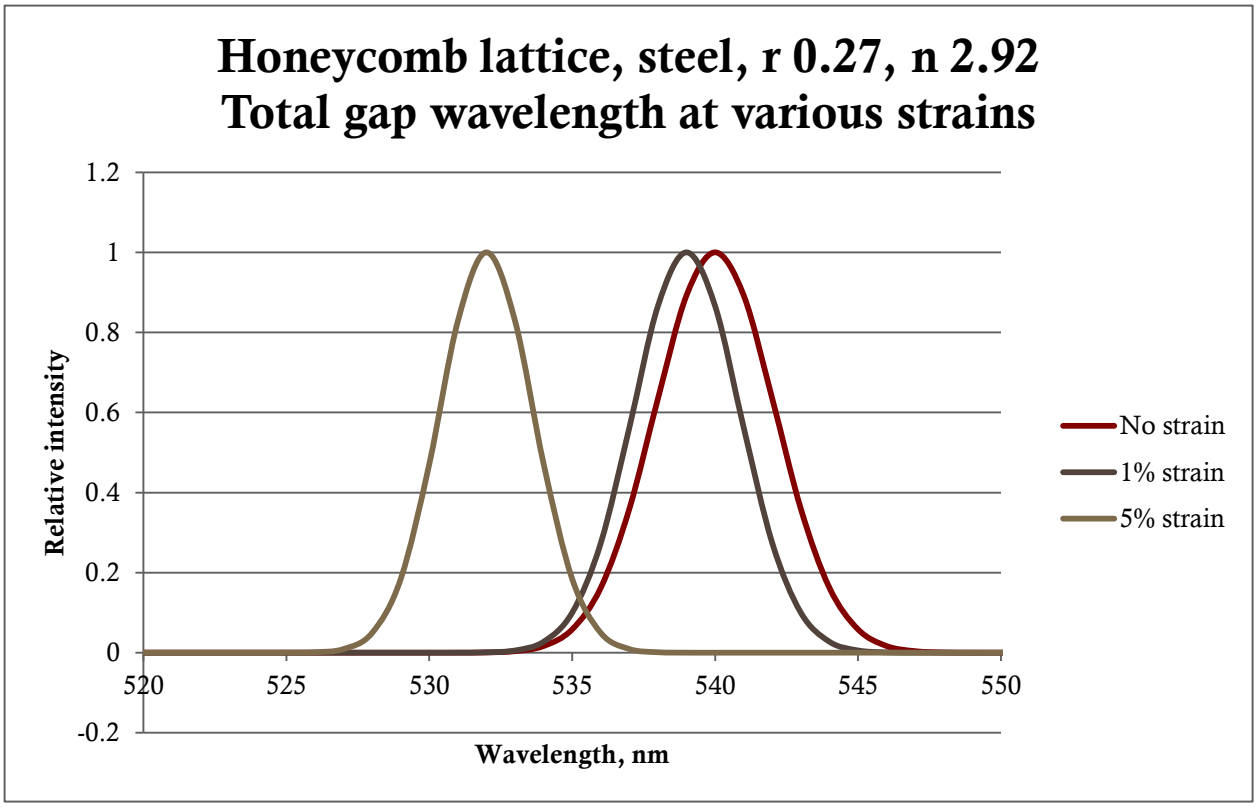
Honeycomb lattice, steel, r 0.27, n 2.92
Total gap wavelength at various strains
Relative intensity
1.2
1
0.8
0.6
0.4
0.2
0
-0.2
520
525
530
535
540
545
550
Wavelength, nm
No strain
1% strain
5% strain